ARTICLE IN PRESS

Nature Communications

https://doi.org/10.1038/s41467-026-73132-x

Article in Press

Two-dimensional HRS condensates drive the assembly of flat clathrin lattices on endosomes

Received: 9 May 2025

Accepted: 28 April 2026

Cite this article as: Hakala, M., Moparthi, S.B., Ganeva, I. *et al.* Two-dimensional HRS condensates drive the assembly of flat clathrin lattices on endosomes. *Nat Commun* (2026). https://doi.org/10.1038/s41467-026-73132-x

Markku Hakala, Satish Babu Moparthi, Iva Ganeva, Mehmet Gül, César Bernat-Silvestre, Carlos Marcuello, Javier Espadas, Adai Colom, Mikhail Kudryashev, Wanda Kukulski, Stéphane Vassilopoulos, Marko Kaksonen & Aurélien Roux

We are providing an unedited version of this manuscript to give early access to its findings. Before final publication, the manuscript will undergo further editing. Please note there may be errors present which affect the content, and all legal disclaimers apply.

If this paper is publishing under a Transparent Peer Review model then Peer Review reports will publish with the final article.

ARTICLE IN PRESS

© The Author(s) 2026. **Open Access** This article is licensed under a Creative Commons Attribution-NonCommercial-NoDerivatives 4.0 International License, which permits any non-commercial use, sharing, distribution and reproduction in any medium or format, as long as you give appropriate credit to the original author(s) and the source, provide a link to the Creative Commons licence, and indicate if you modified the licensed material. You do not have permission under this licence to share adapted material derived from this article or parts of it. The images or other third party material in this article are included in the article's Creative Commons licence, unless indicated otherwise in a credit line to the material. If material is not included in the article's Creative Commons licence and your intended use is not permitted by statutory regulation or exceeds the permitted use, you will need to obtain permission directly from the copyright holder. To view a copy of this licence, visit http://creativecommons.org/licenses/by-nc-nd/4.0/.

ARTICLE IN PRESS

Two-dimensional HRS condensates drive the assembly of flat clathrin lattices on endosomes

Markku Hakala[1,2], Satish Babu Moparthi[3], Iva Ganeva[4], Mehmet Gül[5,6], César Bernat-Silvestre[1], Carlos Marcuello[7], Javier Espadas[1], Adai Colom[7], Mikhail Kudryashev[5,8], Wanda Kukulski[4], Stéphane Vassilopoulos[3], Marko Kaksonen[1#], Aurélien Roux[1#]

[1] Department of Biochemistry, University of Geneva, Switzerland

[2] Helsinki Institute of Life Sciences and the Institute of Biotechnology, University of Helsinki, Finland

[3] Sorbonne Université, INSERM, Institute of Myology, Centre of Research in Myology, UMRS 974, Paris, France.

[4] Institute of Biochemistry and Molecular Medicine, University of Bern, Bern, Switzerland

[5] In situ Structural Biology, Max Delbrück Center for Molecular Medicine in the Helmholtz Association (MDC), Berlin, Germany

[6] Institute of Chemistry and Biochemistry, Freie Universität Berlin, Germany

[7] Biofisika Institute (CSIC, UPV/EHU) and Department of Biochemistry and Molecular Biology, University of the Basque Country, Leioa, Spain

[8] Institute of Medical Physics and Biophysics, Charité-Universitätsmedizin Berlin, Germany

Correspondence to Aurelien.Roux@unige.ch, and Marko.Kaksonen@unige.ch.

ARTICLE IN PRESS

Abstract

In cells, the curved clathrin structures in vesicle budding are well characterized, while the flat ones remain poorly understood. Here, we reconstitute the flat assembly of ESCRT-0 protein HRS and clathrin onto lipid membranes *in vitro*. HRS forms gel-like protein condensates at micromolar concentrations in solutions. These condensates spread as a two-dimensional layer on negatively charged membranes and, together with clathrin, form multilayered coats. Importantly, the two-dimensional condensates spontaneously form only on membranes at HRS concentrations below 50nM, its cytoplasmic concentration. Correlative cryo-electron tomography of HRS-labelled endosomes in cells reveals a multilayered structure containing a flat clathrin layer 16 nm away from the membrane, consistent with our *in vitro* findings. Cholesterol enhances HRS recruitment to the membrane both in cells and in supported bilayers. Furthermore, cholesterol promotes the phase separation of HRS onto membranes, which in turn concentrates cholesterol underneath. This positive

ARTICLE IN PRESS

feedback promotes the formation of HRS-clathrin microdomains that sorts reconstituted ubiquitinated cargoes. Altogether, our results show that the distinct architecture of ESCRT-0 is assembled by the two-dimensional phase-separation of HRS which drives the assembly of flat clathrin coats.

ARTICLE IN PRESS

ARTICLE IN PRESS

Introduction

Clathrin, the main component of the coat involved in clathrin-mediated endocytosis (CME), self-assembles i*n vitro* into spherical cages that resemble the coats observed on endocytic vesicles [1–5]. During CME, membrane-binding adaptor proteins drive clathrin assembly into hexagons and pentagons, promoting membrane deformation and invagination [6,7]. Besides CME, clathrin is involved in intracellular vesicle trafficking routes between endosomes, trans-Golgi network, and the plasma membrane. During these trafficking processes, the clathrin coat assembles on the organellar membrane and facilitates membrane budding in a similar way to CME [8]. In addition to vesicular clathrin structures that promote membrane deformation, mammalian cells have flat and tubular clathrin structures, which are not linked to vesicle trafficking [8]. At the plasma membrane, hexagonal clathrin lattices participate in the formation of integrin-dependent adhesion plaques or collagen-pinching tubular adhesions [9–11].

Among the flat clathrin lattices, the least characterized are found on endosomes. There, clathrin associates with the endosomal sorting complex required for transport (ESCRT)-0 by binding with Hepatocyte growth factor tyrosine kinase substrate HRS/HGS (from now on, HRS) [12,13]. HRS has a ubiquitin-binding VHS (VPS27/HRS/STAM) domain, a PI(3)P (phosphatidylinositol 3-phosphate)-binding FYVE domain, a double ubiquitin binding motif, and a helical domain [14–16]. The C-terminus of HRS contains a clathrin box motif, which interacts with the clathrin heavy chain [12]. On endosomes, HRS-clathrin domains sort ubiquitylated cargoes, which are further concentrated into intraluminal vesicles (ILV) [17–19]. Remarkably, HRS-clathrin coats have a distinctive bi-layered organization [13], which is distinct among clathrin structures in the cell [8]. How the distinct architecture of the ESCRT-0-clathrin coat is assembled on endosomes and how it is linked to its sorting function remains unanswered.

Cholesterol is highly abundant in membranes where clathrin-mediated trafficking occurs: the trans-Golgi network, endosomes, and the plasma membrane [20,21]. Cholesterol plays a crucial role in lipid phase separation and sets membrane biophysical properties, making it essential for numerous membrane functions. For example, cholesterol concentration in the membrane correlates with the membrane bending during CME [22–24]. Cholesterol is highly enriched in multivesicular endosomes [25,26], and its trafficking in cells is tightly regulated [27,28]. An imbalance of this tight regulation causes diseases, as the excess of cholesterol in endosomes alters transport functions in the Niemann-Pick type C disease caused by mutations in *NPC1* or *NPC2* genes [29,30]. However, the physiological roles of

ARTICLE IN PRESS

cholesterol at endosomes remain poorly characterized. Furthermore, while both cholesterol and clathrin are enriched in the same membrane compartments, whether the cholesterol and clathrin assembly impact each other has not been investigated.

Here, we study the assembly of ESCRT-0-clathrin coats on endosomes and their interplay with the underlying membrane. Our reconstitution approach shows that HRS recruitment to the membrane depended on its interaction with PI(3)P and was enhanced by cholesterol. HRS, which contains unstructured domains, forms spherical condensates in solution and two-dimensional condensates on membranes. Two-dimensional HRS condensates promote the assembly of multilayered clathrin coats that contain both flat and shallow pit clathrin structures. In cells, the recruitment of HRS and clathrin on endosomes also depends on cholesterol, and cryo-electron tomography shows that clathrin forms a flat, hexagonal lattice.

ARTICLE IN PRESS

ARTICLE IN PRESS

Results

HRS condensates form thin coats on supported lipid bilayer membranes

We first aimed to understand the recruitment of HRS onto membranes. Its FYVE domain binds phosphatidyl-inositol 3-phosphate (PI(3)P), which is enriched in early endosomal membranes and intraluminal vesicles [14,31,32]. As expected, HRS was recruited onto giant unilamellar vesicle (GUV) membranes containing 1 mol% PI(3)P, 44 mol% DOPC, 20 mol% DOPS, 20 mol% DOPE, and 15 mol% cholesterol (Lipid mix 1, Supplementary Table 2), but not onto membranes lacking PI(3)P (Lipid mix 2, Supplementary Table 2) (Figure 1a). To test the recruitment kinetics of HRS onto PI(3)P-rich membranes, we prepared supported lipid bilayers (SLBs) with 1% PI(3)P (Lipid mix 1, Supplementary Table 2) and followed the recruitment of labeled HRS using total internal reflection fluorescence (TIRF) microscopy (Figure 1b). Recruitment of HRS followed single exponential kinetics, saturating after 15-20 minutes with 100 and 250 nM bulk HRS and significantly faster with 500 nM bulk HRS (Figure 1c). 100 nM bulk HRS led to a protein coat on the membrane that showed moderate fluorescence recovery after photobleaching, an indication of lateral protein movement on the membrane after recruitment. In contrast, at 250 nM and 500 nM bulk HRS, the recruitment led to a stable protein coat with minimal lateral movement (Supplementary Fig. 1a).

We then attempted to study HRS recruitment on membranes with higher protein concentrations. Surprisingly, using 2 μM bulk HRS concentration, spherical protein droplets formed in near physiological salt solution (Figure 1d, Supplementary Fig 1b). These droplets could grow by fusion and coalescence (Figure 1d, Supplementary Movie 1), suggesting they are biomolecular protein condensates. Unlike conventional liquid-like condensates [33], their fusion time was relatively long (Figure 1d). Moreover, they did not show a rapid recovery upon photobleaching (Figure 1e). These observations suggested that HRS forms gel-like protein condensates [34].

We wondered how these condensates would interplay with membranes. To test this, we introduced 2 μM labeled HRS on SLBs containing 1% PI(3)P (Lipid mix 1, Supplementary Table 2). The protein condensates interacted with the membrane and started spreading on it (Figure 1f, orange arrows). Eventually, the protein droplets spread entirely on the membrane surface and fused into a continuous and homogenous layer of HRS fully covering the membrane (Figure 1f, orange arrows) (Supplementary Movie 2). Supporting our conclusion that HRS forms gel-like condensates, the mixing rate of fusing droplets and spreading of condensates onto the membranes was relatively low, in a time

ARTICLE IN PRESS

scale of tens of minutes. The fluorescence intensity of HRS remained rather constant throughout the wetted area, indicating that the HRS layer that spreads onto the membrane forms a two-dimensional film (Supplementary Fig. 1c). To test if the protein can diffuse in HRS condensates on the membrane, we photobleached small regions of the droplet-like condensates, and of the condensate film spread on the membrane (Supplementary Fig. 1d). Similarly to the HRS droplet condensates, two-dimensional condensates spreading on membranes did not show a fluorescence recovery in the photobleached region within the 3-minute acquisition period (Figure 1e, Supplementary Fig. 1d), further indicating the viscous, gel-like properties of HRS condensates also on membranes.

When we incubated SLBs containing 1% PI(3)P (Lipid mix 1, Supplementary Table 2) with 2 μM HRS, we noticed the spontaneous formation of HRS domains with the same intensity as the two-dimensional condensate spreading out from droplets (Figure 1f, yellow arrowheads, Figure 1g). This suggested that, in addition to droplet-like condensates spreading on membranes, the two-dimensional condensates can form directly on the membrane surface from the free HRS pool in solution. We speculated that the HRS microdomains we observed on GUV membranes in 250 nM bulk HRS concentration (Figure 1a) could be a result of membrane-bound HRS phase-separation, and not only the spreading of already phase-separated HRS droplets. Indeed, membranes restrict protein diffusion in two dimensions and concentrate proteins, promoting their phase separation [35]. To test this possibility, we monitored phase separation on GUVs and in bulk at different HRS concentrations. We observed HRS microdomain formation on GUVs already at 10 and 20 nM bulk protein concentrations (Figure 1h), a concentration much lower than the threshold concentration of bulk phase-separation (>500 nM). To compare these values with the concentration of cytosolic HRS in cells, we tagged endogenous HRS in HeLa MZ cells with mScarlet-I3 fluorescent protein using CRISPR-Cas9 (see Methods, CRISPR-Cas9 knock-in cell lines). We confirmed the correct localization of mScarlet-I3-HRS by labeling endosomes and lysosomes with a pulse of AlexaFluor-647 labeled epidermal growth factor (AF647-EGF) [18] (Supplementary Fig. 2c-d). We then compared the fluorescence intensity of the cytoplasmic pool of mScarlet-I3-HRS in CRISPR cells to purified Scarlet-I3-HRS protein solutions of known concentration (Supplementary Fig. 2e-f). These measurements indicated that the cytoplasmic concentration of HRS in CRISPR cells is around 50 nM. We however note that the total protein amount in our CRISPR cell is only around 10% of the wild type HRS expression (Supplementary Fig. 2g). Therefore, the cytoplasmic concentration of HRS in wild type cells is likely in the range of 50-500 nM, concentrations at which HRS phase-separates onto membranes but not in the solution.

ARTICLE IN PRESS

High-energy interactions with membranes are known to favor complete membrane wetting by protein condensates [36]. Thus, the strong interaction between HRS and lipids in the SLBs could promote wetting behavior. We tested this by observing whether the protein condensates spread on a membrane composed of DOPC lipids only (uncharged membrane, Lipid mix 7, Supplementary Table 2) or a membrane containing negatively charged DOPS as well as PI(3)P and cholesterol (Lipid mix 1, Supplementary Table 2). HRS condensates did not adhere nor spread on the DOPC-only membranes but readily spread on the DOPS/PI(3)P/cholesterol-rich membrane as well as membranes containing 20% DOPS and cholesterol but no PI(3)P (Lipid mix 2, Supplementary Table 2), forming a dense protein film (Supplementary Fig. 1e). Therefore, we concluded that electrostatic interactions of HRS with charged lipids were essential for membrane wetting and growth of the two-dimensional condensate.

To better understand the formation of HRS condensates on membranes, we used high-speed atomic force microscopy (HS-AFM). When 500 nM HRS was injected into the imaging chamber containing SLBs on mica, we initially observed a homogeneous binding of HRS (Figure 2a, timepoint 39 min), which slowly separated into patches (Figure 2a, timepoint 61 min). Similar to HRS patches imaged with fluorescence microscope (Figure 1b,g), HRS patches in our AFM experiments grew over time with larger protein patches being less mobile (Supplementary Movie 3). This supports the low protein diffusion observations done by FRAP (Supplementary Fig. 1a,d). HS-AFM also allowed us to measure the thickness of the HRS patches to be around 10 nm (Figure 2b).

ARTICLE IN PRESS

Unstructured regions and the helical domain promote phase-separation of HRS

HRS has three structured domains: N-terminal VHS and FYVE domains, and the helical domain in the middle of the protein (Figure 2c). Alphafold3 [37] and IUPred3 [38] predict that the rest of the peptide sequence is unstructured (Supplementary Fig. 3a-b). We evaluated the propensity of these unstructured regions to promote phase separation with multiple different prediction algorithms [39–41]. These tools predicted that regions between the residues 220-403 and 503-777, and in particular the prion-like region at the C-terminus, promote the phase separation (Figure 2c, Supplementary Fig 3c).

To experimentally test which of these HRS regions are important to form condensates, we overexpressed GFP-tagged full-length HRS and truncated proteins in HeLa MZ cells (Figure 2d). As expected, the GFP-tagged full-length HRS (residues 1-777) formed droplet-like condensates when

ARTICLE IN PRESS

overexpressed in HeLa cells (Figure 2d). These condensates underwent fusion events and co-localized with an endosome marker, AlexaFluor 647 -labelled EGF (Figure 2e-f). Expressing GFP-VHS and GFP-FYVE (residues 1-220) showed only a diffuse cytoplasmic signal. Contrastingly, overexpression of the GFP construct lacking VHS and FYVE domains but containing all the predicted unstructured regions and the helical domain (residues 221-777), led to the formation of fluorescent condensates similar to the full-length protein (Figure 2d). These condensates underwent slow fusion events (Supplementary Movie 4) and recovered slowly after photobleaching (Supplementary Fig 3d). When we expressed the HRS construct containing residues 221-403, diffuse cytoplasmic signal was observed, phenocopying the HRS 1-220 construct. GFP-HRS 221-503 showed some propensity to form condensates in cells along strong cytoplasmic signal, indicating that the helical domain between residues 403-503 is also important for condensate formation. Finally, when we expressed GFP-HRS constructs lacking the helical domain (1-777 Δhelix or 221-777 Δhelix), we observed a strong cytoplasmic signal with a weak propensity to form condensates (Figure 2d).

From these findings, we concluded that both prion-like unstructured regions between residues 503-777 and the helical domain are needed for HRS condensates to form.

HRS recruits clathrin on membranes as flat coats and domes

Since clathrin does not directly bind to membranes, the formation of various clathrin structures on cellular membranes relies on organelle-specific adaptors, with HRS being one of the adaptors associated with endosomes. Here, we used clathrin purified from bovine brains. Notably, bovine clathrin is structurally similar to human clathrin (99.94% sequence similarity for clathrin heavy chain 1). We measured the dynamics of clathrin recruitment on HRS-coated supported lipid bilayer (SLB) membranes containing 1 mol% PI(3)P, 44 mol% DOPC, 20 mol% DOPS, 20 mol% DOPE, and 15 mol% cholesterol (Lipid mix 1, Supplementary Table 2) by using sequential addition of proteins (Figure 3a-b). Our experiments revealed that HRS recruits clathrin on SLBs in a concentration-dependent manner (Figure 3c-e) with both the nucleation rate and the final amount of membrane-bound clathrin proportional to the bulk HRS concentration (Figure 3d-e). Clathrin recruitment followed a single exponential kinetics but did not saturate at high HRS concentrations.

Our reconstitution experiments indicated that HRS promotes clathrin recruitment in a concentration-dependent manner. In the next step, we wanted to visualize these HRS-clathrin coats at a higher resolution. Platinum replica electron microscopy (PREM) is a powerful approach to visualize protein

ARTICLE IN PRESS

lattices on flat surfaces because it provides high contrast and shadowing [42–44]. With 100 nM HRS, we observed small, flat clathrin patches on SLBs (Figures 3f, Supplementary fig 4a). These patches were often accompanied by spherical clathrin cages. Because these cages were always connected to a neighboring clathrin patch (Figure 3f), we reasoned that they originated from initially flat clathrin lattices or were assembled as cages next to flat protein patches. With 500 nM HRS and 200 nM clathrin, we frequently observed large patches of flat and dense clathrin islands along with regions where clathrin formed shallow pits and dome-shaped structures with various curvatures (Figure 3g, Supplementary fig 4b).

We then wanted to measure the thickness of the HRS-clathrin coat. To this end, we reconstituted 500 nM HRS and 200 nM clathrin on SLBs on the mica surface and imaged them with HS-AFM (Figure 3h, Supplementary Movie 5). While the thickness of HRS condensates in the absence of clathrin was 10 nm (Figure 3i), clathrin assembled on two-dimensional HRS condensates yielded a coat with a median thickness of 17 nm (Figure 3i).

ARTICLE IN PRESS

HRS and clathrin assemble as multilayered coats

We often observed round clathrin islands in our PREM samples prepared with 500 nM of HRS and 200 nM of clathrin (Figures 4a). The clathrin islands had a dense and predominantly flat appearance. They appeared as stacked flat patches coated with clathrin, having multiple layers of similar thickness (Figure 4b-c). The electron opacity increased gradually, doubling in each new layer, indicating that these layers contain multiple layers of clathrin (Figure 4c). The observation of flat clathrin patches raised the question of how they are formed. Tilt series of this PREM sample showed that these patches are thicker than a clathrin coat alone, suggesting that they are formed on top of a thick protein coat (Supplementary Movie 6). To test whether this multilayering feature arises from multiple layers of HRS condensates or if multilayering is induced by the re-organization of HRS condensates during clathrin assembly, we visualized HRS condensates alone on SLBs by PREM. We occasionally observed large, multilayered HRS condensates (Figure 4d, Supplementary Movie 7), supporting the notion that two-dimensional HRS condensates can eventually stack up into multilayered coats, leading to multilayered clathrin islands.

Consistent with our observations of different layers in HRS-clathrin structures, HRS-clathrin coats imaged with HS-AFM had regions with different thicknesses (Supplementary Fig 5a). The thickness

ARTICLE IN PRESS

of the thicker regions was around 15-30 nm, while the thickness of the thinner ones was 8-15 nm (Supplementary Fig 5b), consistent with the stacking of layers (Figure 4b). We observed hexagonal and pentagonal clathrin structures, especially in the thicker regions (Supplementary Fig 5c), while the thinner regions appeared to contain less structured clathrin coats (Supplementary Fig 5d). This supports the notion that the HRS-clathrin assembly is multi-layered, and that the clathrin is assembled into flat coats primarily on the thinner regions, corresponding to a single, two-dimensional HRS condensate.

Clathrin assembly varies depending on the type of HRS condensates it binds to

We wondered how HRS condensates modify the structure and dynamics of clathrin assembly compared to the low density of HRS on the membrane. To test this, we incubated PI(3)P-rich SLBs (Lipid mix 1, Supplementary Table 2) with 2 μM HRS. Immediately after droplet-like condensates formed, we washed the remaining HRS out five times and introduced 200 nM of clathrin. Droplet-like HRS condensates readily recruited clathrin, which did not enter inside the condensates but covered the surface of the protein condensate (Supplementary Fig 6a). To investigate how clathrin binds to two-dimensional condensates, we used the same protocol but waited until the spreading of two-dimensional condensates occurred before adding clathrin. Fluorescent clathrin was recruited both onto HRS droplets that had not fully spread into two-dimensional condensates, as well as onto two-dimensional condensates (Supplementary Fig 6b). In confocal fluorescence microscopy images, we observed that HRS fluorescence intensity increased stepwise from the low-density region to high-density two-dimensional condensate and dramatically increased at the droplet-like condensate (Supplementary Fig 6b-c). Clathrin fluorescence intensity followed the same trend (Supplementary Fig 6b-c).

We looked at the clathrin coat architecture on droplets and two-dimensional condensates using PREM. Platinum replica samples prepared with 2 μM HRS and 200 nM clathrin showed extensive amounts of clathrin cages at the surface of HRS droplets (Figures 5a and Supplementary Fig 6d-f). Clathrin structures at the surface of two-dimensional condensates next to the droplet condensates appeared flatter and less numerous than on droplets (Figures 5b and Supplementary Fig 6f). Furthermore, we observed areas where flat clathrin lattices were visible (Figures 5b and Supplementary Fig 6f). These flat clathrin lattices were similar to those we observed at 500 nM HRS concentration (Figure 4a), supporting the hypothesis that these dense, round-shaped patches of flat clathrin are assembled on two-dimensional HRS condensates.

ARTICLE IN PRESS

Taken together, our fluorescence microscopy data with HRS condensates and labeled clathrin support the idea of three different HRS populations on the membrane: 1) low-density HRS, 2) two-dimensional HRS condensates, and 3) droplet-like HRS condensates, which all readily recruit clathrin (Figure 5c). Gel-like, two-dimensional condensates promote the assembly of both flat, dense clathrin coats as well as minimally curved clathrin pits. On the other hand, HRS droplets promoted clathrin assembly into highly curved coats and spherical cages. Finally, we observed multilayered clathrin coats on HRS condensates. The exact mechanism of this stacking remains to be studied. We next wondered how similar these *in vitro* clathrin assemblies mediated by condensation of HRS are compared to the in vivo ESCRT-0 assemblies found on endosomes.

Correlative cryo-electron tomography of cells reveals a three-layered protein coat including a hexagonal clathrin lattice on endosomes

Previous studies have identified flat clathrin microdomains on endosomes by electron microscopy of resin-embedded cells [13,17]. However, these studies did not visualize the clathrin coat architecture. We aimed to reveal endosomal clathrin lattices using cryo-electron tomography combined with subtomogram averaging, a workflow to image and structurally analyze molecules in situ. We used cryo-correlative light and electron microscopy (cryo-CLEM) to identify HRS-positive endosomes and acquire tilt series at these spots (Supplementary Fig 7a-d) in the Scarlet-I3-HRS HeLa cells and in a previously described HeLa cell line stably expressing mCherry-HRS [18,19]. In the resulting tomograms of areas targeted by either mCherry-HRS, mScarlet-I3-HRS, or Alexa-Fluor-647 labeled EGF signals, we observed patches of a dense protein coat on endosomes (Figures 6a and Supplementary Fig 7e-p). This coat extended approximately 40-60 nm from the membrane (Figure 6a, yellow brackets). Consistent with previous reports [13,17], we found this protein coat to have a flat and multi-layered appearance, similar to the structures we observed in our reconstituted samples by PREM and HS-AFM (Figure 6b-c, yellow arrows).

We next used subtomogram averaging to further analyze the organization of the coat (Supplementary Fig 8a-d). This approach revealed a three-layer arrangement of the coat (Figure 6d-e). The first layer was positioned 16 nm from the endosomal membrane and showed a periodical pattern. Subsequent layers were positioned 18 nm and 14 nm above the previous layers (Figure 6d). The distance of the first layer from the membrane was similar to the thickness of HRS-clathrin assemblies measured by HS-AFM (Figure 3i). The averaging indicated that the predominant feature of the first layer was a hexagonal lattice. We therefore applied a six-fold symmetry, which revealed a lattice constant (vertex-

ARTICLE IN PRESS

to-vertex length) of 24-26 nm (Figures 6f and Supplementary Fig 8e). These dimensions and the hexagonal organization are typical for flat clathrin lattices [45–47], indicating that this layer corresponds to a flat clathrin coat. However, we point out that because of the averaging techniques, the lattice may not be as regular as seen in the averages. A coat that is to a large extent unstructured but contains hexagonal elements, as seen by PREM, can result in a fully ordered, hexagonal average structure. The same analysis of the second and the third layers did not reveal periodical arrangements that would be indicative of a lattice-like structure.

Our *in vitro* reconstitution data show that HRS readily forms large, multi-layered assemblies of clathrin on PI(3)P-rich membranes. The appearance and dimensions of these reconstituted HRS-clathrin coats are similar to the multilayered coats we found on endosomes in cells that include a predominantly hexagonal clathrin architecture. We next asked what regulates the formation of these multilayered HRS-clathrin domains on endosomes and focused on the properties of the underlying membrane.

Cholesterol enhances HRS and clathrin recruitment on endosomes in cells

Cholesterol is prominent at endosomes and other organelles where clathrin assembles [20,21,25]. Therefore, we decided to test its role in clathrin assembly on endosomes. HRS forms distinct domains on endosomes [17,48] and we tested if these HRS domains are rich in cholesterol. We stained cholesterol in the mScarlet-I3-HRS cells with Filipin and observed colocalization of HRS with cholesterol (Figure 7a). We then tested whether cholesterol levels affect the recruitment of HRS to endosomes. To this end, we used HeLa cells knock-out for the *NPC1* gene [49], which encodes a lysosomal cholesterol transporter whose depletion elevates cholesterol in endosomal compartments [50,51] (Figure 7b), and immuno-stained them against endogenous HRS and clathrin (Figure 7c). NPC1-KO cells displayed an increase in endosome-bound HRS-clathrin compared to control cells, as seen from the significant increase in both HRS intensity (Figure 7d) and puncta size (Figure 7e), as well as clathrin fluorescence intensity (Figure 7f). We confirmed that HRS was still localized to endosomes in NPC1-KO cells, as endogenous HRS predominantly colocalized with EEA1, a marker of early endosomes, but not with LAMP1, a marker for lysosomes (Supplementary Fig 9a-b). We also analyzed the HRS localization in cells treated with U18666A drug, an inhibitor of NPC1 [52]. Similar to NPC1-KO cells, U18666A-treated cells showed increased HRS signal in the endosomes (Supplementary Fig 9c), while no change in HRS localization was observed (Supplementary Fig 9d-e).

ARTICLE IN PRESS

We concluded from these data that HRS binds to endosomal membranes in correlation with their cholesterol content. To further understand the role of cholesterol in assembling HRS-clathrin coats, we tested its role in our *in vitro* reconstitution assay.

***Cholesterol promotes the assembly of the HRS*-clathrin coat**

We tested the recruitment of HRS on GUVs containing 1% PI(3)P and varying cholesterol concentrations: 0%, 15%, and 30% cholesterol (Lipid mixes 3, 1, and 4, respectively, Supplementary Table 2). Cholesterol enhanced the recruitment of HRS on membranes (Figure 8a,c) and correspondingly, more clathrin was recruited on HRS-positive GUVs containing increasing amounts of cholesterol (Figure 8b,d). Interestingly, with 0% and 15% cholesterol, HRS was recruited on the membrane as small patches, whereas on membranes with 30% cholesterol, HRS either formed larger patches or covered the whole GUV membrane. We wondered if cholesterol could also promote the wetting of SLB membranes by HRS condensates. To test this, we prepared SLBs with varying cholesterol concentrations as above (0%, 15%, or 30% cholesterol) and tested the membrane wetting by using 2 μM fluorescently labeled AF488-HRS (Figure 8e). We observed a significant increase in membrane wetting with higher cholesterol concentrations (Figure 8f).

One of the key features of clathrin coats, especially when related to membrane trafficking, is their ability to bend the membrane. In our reconstitution samples imaged with PREM, we observed both flat clathrin patches as well as regions where clathrin formed dome-shaped structures (Figures 3f-g, 4a-b, 5a-b). Consistent with the cryo-electron tomography data, we did not observe membrane deformation upon HRS-clathrin coat assembly on GUV membranes (Figure 8b). GUV membranes cannot be remodeled when membrane tension is too high, but lowering the tension through osmotic shocks promotes membrane remodeling by clathrin coats [53]. To test the membrane remodeling properties of HRS-clathrin assemblies under low membrane tension, we coated GUVs with HRS and clathrin and then lowered the membrane tension with hyperosmotic shocks. HRS and clathrin reconstituted on GUVs containing 0% or 15% cholesterol and subjected to osmotic shock did not change shape (Figure 8g). In contrast, hyperosmotic shocks induced GUV flattening when HRS and clathrin were reconstituted on GUVs containing 30% cholesterol (Figure 8g). Such flattening, which appeared as facets on the GUVs (Figure 8h) and gives the GUV contour the appearance of a segmented line with vertices, was previously observed with protein assemblies that preferred low curvature areas, such as Snf7 [54,55]. Importantly, hyperosmotic shock did not lead to membrane deformations of GUVs without proteins or those incubated only with HRS (Supplementary Fig 10a-

ARTICLE IN PRESS

b). Taken together, our experiments show that reconstituted HRS-clathrin coats are flat and, under low membrane tension, induce the flattening of membranes (Figure 8g-h). This is consistent to our cryo-electron tomography data (Figure 6), and in striking contrast with endocytic clathrin adaptor AP180 and clathrin that yielded prominent outward-directed budding assemblies upon hyperosmotic shocks [53].

Cholesterol clusters and diffuse more slowly under the HRS-clathrin coat

The finding that cholesterol enhances HRS wetting on the membrane led us to speculate that HRS could promote the formation of cholesterol-rich domains. This hypothesis could be assessed with a fluorescence quenching assay, which relies on the property of the TopFluor probe to self-quench at high density due to a fluorescence resonance energy transfer (FRET) between neighboring probe molecules (Figure 9a)[56]. We prepared large unilamellar vesicles (LUVs) with 1% PI(3)P and 30% cholesterol supplemented with 0.1% TopFluor-cholesterol (Lipid mix 6, Table 2) and measured the fluorescence intensity of these vesicles with increasing concentrations of HRS in a spectrophotometer. TopFluor fluorescence decreased as a function of HRS concentration (Figure 9b), supporting the hypothesis that HRS clusters cholesterol. We then used SLBs labeled with 1% TopFluor-cholesterol (Lipid mix 5, Supplementary Table 2) and tested if cholesterol gets enriched under HRS and clathrin. While it may look incoherent that HRS-dependent clustering of TopFluor-Cholesterol leads to global fluorescence quenching at the same time as fluorescence increase under the HRS domains, the lateral segregation of cholesterol under HRS domains could lead to apparition of fluorescent domains while promoting quenching because of the increased cholesterol density in HRS domains. Cholesterol was enriched under protein domains formed by both HRS condensates alone as well as HRS condensates incubated with clathrin (Figure 9c), supporting our hypothesis that cholesterol-rich domains form under HRS and HRS-clathrin patches.

The clustering of cholesterol underneath the HRS-clathrin coat should be associated with reduced diffusion, which can be measured by FRAP [57]. To test this, we incubated membranes containing 1% TopFluor-cholesterol (Lipid mix 5, Supplementary Table 2) with 500 nM HRS and 200 nM clathrin and photobleached small regions of membrane under the HRS condensates. Compared to the control without proteins, TopFluor-cholesterol showed a reduction of diffusion in samples incubated with HRS. The sterol diffusion was reduced even more when these samples were incubated also with clathrin, suggesting that clathrin might reorganize the HRS coat, which further increases the stability

ARTICLE IN PRESS

of the underlying membrane. (Figure 9d-f). These experiments indicate that HRS-clathrin coats decrease membrane fluidity and form cholesterol-rich, stable membrane domains, suggesting that lipid phase separation could be coupled to HRS-clathrin assemblies.

HRS coats on cholesterol-rich membrane cluster cargo proteins

The main function of ESCRT-0 is to sort ubiquitylated cargoes into ILVs [17,19,58]. We thus wondered whether HRS-clathrin could promote cargo clustering in our *in vitro* assay. To test this, we used the VAMP2 protein, a transmembrane cargo model for ESCRT-0 in previous studies [59]. We purified a recombinantly expressed VAMP2 chimera with four ubiquitin moieties at its N-terminus and sfGFP at its C-terminus and reconstituted it into the GUV membrane (see Methods, Cargo protein reconstitution and clustering, and Figure 10a). To test the effect of cholesterol on cargo clustering, we prepared cargo-containing membranes either with or without cholesterol (Lipid mixes 3 and 4, respectively, Supplementary Table 2). Without HRS, Ub-VAMP2-GFP showed mostly homogenous distribution in GUVs (Figure 10b). When we incubated these cargo-containing GUVs with HRS, cargo clusters appeared to be larger in membranes containing 30% cholesterol compared to those without cholesterol (Figure 10c). HRS-VAMP2 clusters on membranes containing 30% cholesterol appeared to be more stable, indicated by their negligible lateral movement over time (Figure 10d, Supplementary Movie 8), whereas HRS-VAMP2 clusters on membranes without cholesterol were small and showed higher lateral movement (Figure 10e, Supplementary Movies 9). These observations indicate that cholesterol domains promote HRS-clathrin cargo clustering and stabilization of HRS-cargo domains on membranes. Our data thus reveal that HRS-clathrin assemblies are sufficient to sort ubiquitinylated cargoes *in vitro*, and that this clustering is enhanced by cholesterol.

Discussion

While functions of flat clathrin lattices in cellular processes have gathered increased attention during the past years [8], it remains unknown how these structures are assembled in the first place. Here, we reconstituted endosomal, ESCRT-0-driven clathrin coats with minimal components to gain a comprehensive understanding of their assembly mechanism and structural features. We reveal that HRS directly interacts with the membrane, initially forming a low-density protein coat which can phase-separate into a dense, two-dimensional protein film on the membrane (Figure 10f). Clathrin

ARTICLE IN PRESS

assembles on biochemically reconstituted HRS-rich membranes as a dense coat, which is either flat or has different degrees of curved pits and domes. Our experiments with GUVs show that the dense HRS-clathrin coat flattens low-tension membranes, indicating that the flat architecture is a dominant feature of the HRS-clathrin coat. This is in striking contrast to the reconstitution experiments performed with CME-linked clathrin adaptors, which promote membrane bending [53,60,61], highlighting the features of the HRS-clathrin coat among clathrin assemblies.

Cryo-electron tomography of cells revealed flat HRS-clathrin protein coats on endosomes. These coats appeared to be composed of three layers, of which one could be identified as clathrin based on its regular lattice. Thus, the overall coat architecture is different from clathrin structures found on the plasma membrane [8,42,62]. Multilayered protein coats were also observed in previous studies [13,18,19,63,64]. We also observe a layering of the HRS-clathrin coat in our in vitro samples. Notably, two-dimensional HRS condensates and HRS-clathrin coats on SLBs had a thickness of 10 nm and 20 nm, respectively, similar to the distance measured between the membrane and the clathrin lattice on endosomes. Previously observed coat-like densities on endosomes, visualized in sections of resin-embedded cells, had similar dimensions to those in our cryo-electron tomography and reconstitution experiments [63].

Sub-tomogram averaging revealed a hexagonal lattice 16 nm away from the endosome membrane, which resembled other clathrin assemblies imaged in cells [42,45–47,65]. Other arrangements, such as pentagonal elements, might be contained in the lattice but are likely less abundant and thus not represented by the average. We did not observe a distinct protein structure between the clathrin layer and the membrane, where HRS is expected to localize. This observation is in line with HRS forming a two-dimensional condensate, because the intrinsically disordered nature of HRS is not expected to adopt an average structure as the clathrin lattice does. We observed two additional protein layers on top of the hexagonal clathrin lattice. These layers did not show apparent symmetry, and their identity remains to be solved. The flat nature of the HRS-clathrin coat may be due to the higher rigidity, associated with the loss of diffusion, of the two-dimensional HRS condensate that could force clathrin adapt to a flat layer.

Protein phase separation is a phenomenon that has recently been shown to play an important role in membrane remodeling and membrane repair [66–70]. In clathrin-mediated endocytosis, Eps15 and its budding yeast homolog Ede1 were shown to undergo liquid condensation [71,72]. In plants, TSET-TPLATE complex proteins AtEH1 and AtEH2 promote the condensation of the complex [73]. To our best knowledge, HRS is thus far the only protein that was shown to both undergo condensation and

ARTICLE IN PRESS

directly interact with clathrin. Moreover, unlike the above-mentioned proteins, which undergo liquid-liquid phase separation, HRS forms more viscous, gel-like condensates. Our experiments show that a prion-like region at the C-terminus of HRS, as well as the helical domain, are important to form HRS condensates. Thus, HRS and clathrin are distinctive in combining a gel-like protein condensate and a well-structured protein lattice in the same protein assembly. This gives a plausible explanation for why clathrin coats on endosomes have a distinct, multilayered architecture compared to clathrin structures on the plasma membrane and on other organelles. The exact molecular mechanism of this multilayering remains to be studied.

We show that when HRS and clathrin form a protein coat on the membrane, they change the membrane composition by enriching cholesterol under the protein coat (Figure 10f). Here, cholesterol shows lower diffusion, which suggests that HRS and clathrin can promote the formation of cholesterol-rich membrane domains. Since HRS does not contain cholesterol-binding domains or motifs, cholesterol enhances HRS recruitment via an indirect mechanism. Cholesterol was shown to increase the phosphoinositide-dependent membrane interaction with other proteins by clustering phosphoinositides [74]. Moreover, the interaction of protein condensates with membranes is coupled with lipid phase separation [35,75]. We speculate that HRS combines these mechanisms to promote cholesterol clustering and membrane domain formation. HRS-clathrin coats form distinct protein domains on endosomes (Supplementary Fig 9e), which were also reported by other studies [17,18,48,76]. How these protein domains are assembled in the first place and how their size is regulated have remained unanswered questions. We propose that the feedback loop between HRS recruitment and the formation of cholesterol-rich membrane domains facilitates the rise of HRS-positive microdomains on endosomes. Supporting this, the depletion of CD63, a tetraspanin protein that sorts cholesterol to ILVs on endosome membranes [77], results in an unusual abundance of multilayered clathrin coats on multivesicular endosomes [63].

Niemann-Pick C (NPC) 1 and NPC2 proteins at lysosomes are key regulators of cholesterol homeostasis in cells [28,78,79]. Our observation that cholesterol depletion increases the HRS localization at endosomes highlights that cholesterol homeostasis is an important factor regulating ESCRT function and, more globally, the endosomal activity in cells. Sterol depletion at the plasma membrane inhibits membrane bending and vesicle invagination in the CME [22–24,80], which highlights the importance of sterol homeostasis in cells. To our knowledge, the effect of sterols on clathrin adaptor recruitment and clathrin assembly on the plasma membrane has not been studied thoroughly.

ARTICLE IN PRESS

However, it would not be surprising if cholesterol affects clathrin adaptor recruitment on cellular membranes in a similar fashion to HRS. It would thus be interesting to test if clathrin adaptor proteins linked to endocytosis, long-lived plasma membrane clathrin plaques, or reticular adhesions are regulated by sterols.

In conclusion, we show the mechanism of how endosomal protein microdomains of ESCRT-0 and clathrin are formed. The interplay between the cholesterol-rich membranes and HRS condensates facilitates the protein recruitment on the membrane and formation of a cholesterol-rich diffusion barrier in the membrane. This mechanism also provides a platform for cargo clustering under the HRS-clathrin microdomain. Future studies will reveal how cargo proteins are transported from the HRS-clathrin domain to the intraluminal vesicle.

ARTICLE IN PRESS

ARTICLE IN PRESS

Methods

Plasmids and protein purification

All lipids used in this study are commercially available at Avanti Polar Lipids and are listed with their respective catalog numbers in Supplementary Table 1. The vector pCoofy17 was a gift from Sabina Suppmann (Addgene plasmid # 43991)[81]. A plasmid pCS2 HRS-RFP was a gift from Edward de Robertis (Addgene plasmid # 29685). We linearized pCoofy17 with PCR using primers 5'-tccaccggtctgctgctggaacac and 5'- cgccattaacctgatgttctgggg. *HRS* gene was linearized with PCR using primers 5'-gtgttccagcagcagaccggtggaatggggcgaggcagcggcaccttc and 5'-ccccagaacatcaggttaatggcgtcagtcgaatgaaatgagctgg. The pCoofy17-HRS plasmid was subsequently assembled with sequence and ligase independent cloning approach as described in [81]. Plasmids for expression of mScarlet-I3-HRS [pET51(+)-mScarlet-I3-HRS) and 4xUbiquitin-VAMP2-sfGFP [pET28(+)-4xUb-VAMP2-sfGFP] in bacteria, and mScarlet-I3-HRS overexpression in mammalian cells [pcDNA3.1(Zeo+)-mScarlet-I3-HRS] were synthesized and cloned into the destination vector by Gene Universal Inc. Plasmids to overexpress GFP-HRS and truncated proteins [pcDNA3.1(Zeo+)-HRS(1-777), (1-220), (221-403), (221-503), (221-777) and (221-777Δ403-503)] were synthesized by GenScript Inc. All plasmids are available upon request from the corresponding authors.

All recombinant protein expressions were done in BL21 pLysS bacteria either in standard LB media with 0.5 mM IPTG induction or in Autoinduction LB media (# AIMLB0210, Formedium). All proteins were expressed overnight at 20°C. For HRS protein purification, cells were sonicated in HRS lysis buffer (50 mM Tris-HCl, pH 8.0, 500 mM NaCl, 5 mM 2-mercaptoethanol, 300 mM L-arginine) supplemented with PMSF and c0mplete protease inhibitor cocktail (#11697498001, Roche). Soluble protein was then bound to Talon cobalt resin, washed three times with HRS lysis buffer, and then three times with HRS wash buffer (50 mM Tris-HCl, pH 8.0, 500 mM NaCl, 5 mM imidazole, 5 mM 2-mercaptoethanol, 300 mM L-arginine). HRS was cleaved from Sumo3 tag on resin with SenP2 protease in elution buffer (20 mM Tris-HCl, pH 8.0, 500 mM NaCl, 5 mM 2-mercaptoethanol, 300 mM L-arginine pH 7.4). The final protein was cleaned with a Superdex-200 size exclusion column (Cytiva) equilibrated with the elution buffer using Äkta Pure system (Cytiva). A 5% final concentration of glycerol was added to the protein before snap freezing with liquid nitrogen and storage at -80°C.

ARTICLE IN PRESS

To purify VAMP2, cells were lysed in VAMP2 lysis buffer (20 mM Tris-HCl, pH 8.0, 300 mM NaCl, 0.1% Tween-20, 1% Triton X-100, 30 mM imidazole) supplemented with PMSF and c0mplete protease inhibitor cocktail (#11697498001, Roche) using sonicator. Cleared protein lysate was then bound to HisTrap 5 ml HP column and washed with 20 column volumes of VAMP lysis buffer. The protein was eluted with 300 mM imidazole in VAMP lysis buffer and subsequently cleaned with Superdex-200 size exclusion column (Cytiva) equilibrated with the VAMP2 elution buffer (Lysis buffer without imidazole) using Äkta Pure system (Cytiva). A 10% final concentration of glycerol was added to the protein before snap freezing with liquid nitrogen and storage at -80°C. Buffer (Lysis buffer without imidazole) using Äkta Pure system (Cytiva). A 10% final concentration of glycerol was added to the protein before snap freezing with liquid nitrogen and storage at -80°C.

To purify mScarlet-I3-HRS, cells were lysed in HRS lysis buffer supplemented with PMSF and a c0mplete protease inhibitor cocktail (#11697498001, Roche) using Emulsiflex. Protein was then bound to Step-Tactin XT 4Flow resin (Iba Life Sciences). The resin was then washed with HRS lysis buffer, and the protein was eluted with 5 mM biotin in HRS lysis buffer. The final protein was cleaned with Superdex-200 size exclusion column (Cytiva) equilibrated with the HRS elution buffer using Äkta Pure system (Cytiva). A 5% final concentration of glycerol was added to the protein before snap freezing with liquid nitrogen and storage at -80°C.

Clathrin from fresh bovine brains was purified with a standard protocol as described in [82]. Purified clathrin and HRS were labeled with either AlexaFluor-488 or AlexaFluor-568 conjugated C5 maleimide (# A10254 and # A20341, respectively, Thermo Fisher Scientific Scientific) according to the manufacturer's protocol. In all experiments, labelled and unlabelled proteins were mixed in a 20:80 ratio to avoid any unlikely effects of labelling on protein functions.

Reconstitution on giant unilamellar vesicles (GUV)

GUVs were prepared with the gel-assisted swelling method as described in [83] or with silica-bead assisted swelling method. Shortly, PVA (MW 145000, # 8.14894.0101, Sigma-Aldrich) was dissolved at 5% (w/v) in 280 mM sucrose solution. Glass coverslips were cleaned by sonicating them sequentially in water, ethanol, acetone, 1 M KOH and finally in water. A thin layer of dissolved PVA was spread on glass and dried in a 50 °C oven for 30 min. Lipids were mixed in chloroform to the desired composition (Supplementary Table 2) at 1 mg/ml final concentration, and 10 µl of this lipid mixture was spread on PVA gel. Chloroform was then evaporated for 30 min at a 30°C vacuum oven.

ARTICLE IN PRESS

500 µl of swelling buffer (20 mM HEPES, pH 7.4, 50 mM NaCl, osmolarity was adjusted with sucrose) was then added on dried lipids, and GUVs were swelled at room temperature for 30 min.

To prepare GUVs with a silica bead method, we mixed lipids in chloroform at the desired lipid composition (Supplementary Table 2) at 0.5 mg/ml concentration and evaporated chloroform first under argon gas and then in a vacuum for 60 minutes. Lipids were then hydrated with 5 mM Hepes, pH 7.4 buffer, and subsequently mixed with silica beads (# 904384, Sigma Aldrich). Lipids and silica beads were dried in a vacuum for 30 minutes and then prehydrated with 1 M trehalose solution. Prehydrated, membrane-coated silica beads were then transferred in HRS-clathrin reaction buffer (20mM HEPES pH 7.2, 125 mM KAc, 1 mM MgAc).

Protein binding reactions with GUVs were performed in HRS-clathrin reaction buffer (20 mM HEPES pH 7.2, 125 mM KAc, 1 mM MgAc). The osmolarity of the reaction buffer was adjusted to match the reaction buffer and GUV swelling buffer with sucrose, and osmolarity was always measured before experiments with Vapor Pressure Osmometer (Wescor). The osmolarity of the reaction buffer was increased with sucrose for hyperosmotic shock experiments. Labeled proteins were incubated with GUVs in a closed reaction chamber (Ibidi Sticky Slide IV, # 80608, Ibidi GmbH) on a cover glass passivated with either 2 mg/ml BSA in reaction buffer or with PEG-silane. Imaging was performed with a spinning disk confocal microscope (3i Intelligent Imaging Innovations) built on Nikon Eclipse C1 using a 100x 1.3 NA objective. The microscope was controlled with Slidebook 6.0.22 (3i Intelligent Imaging Innovations) and data analysis was performed using Fiji v1.54f. Final graphs were generated with Origin 2024b v10.1.5.132.

ARTICLE IN PRESS

Reconstitution on supported lipid bilayers (SLBs)

To prepare SLBs, we mixed lipids in chloroform and membrane-coated silica beads as described above. Membrane-coated silica beads were then hydrated on plasma-cleaned coverslips attached to Ibidi Sticky Slide IV (# 80608, Ibidi GmbH) in HRS-clathrin reaction buffer (20mM HEPES pH 7.2, 125 mM KAc, 1 mM MgAc). Supported bilayers were spread on glass for 15-30 minutes, and the remaining bare glass areas were passivated with 2 mg/ml BSA in reaction buffer for 60 minutes. The Ibidi slide was connected to a suction pump with a narrow tubing to allow sequential addition of proteins during imaging. After the membrane was washed five times with the reaction buffer, HRS protein was added into the sample chamber in the desired concentration in the reaction buffer. In

ARTICLE IN PRESS

clathrin assembly assays, HRS was incubated on the membrane for 60 minutes before the sample chamber was washed five times with a reaction buffer. Clathrin self-assembles as polyhedral cages in low pH [84], and to avoid unwanted assembly of clathrin cages in solution, all experiments were performed at physiological pH and salt concentrations.

The assembly of labeled HRS and clathrin and fluorescence recovery after photobleaching (FRAP) of assembled protein coats were recorded using an Olympus IX83 TIRF microscope equipped with ImageEM X2 EM-CCD camera (Hamamatsu), Olympus Uapo N 100x NA 1.49 objective. The microscope was controlled with Visiview v.4.4.0.11 software (Visitron Systems). Data was analyzed with Fiji v1.54f. To analyze the recruitment of protein onto SLBs, the intensity of labelled protein was measured in identical-sized region-of interest from each timepoint. The initial background fluorescence before protein addition was then subtracted from every measurement. Data from multiple measurements were pooled, and final graphs with mean fluorescence intensities and standard deviation were generated with Origin 2024b v10.1.5.132. The initial assembly rates (nucleation rates) of clathrin assembly reactions were calculated from the curve angle at the timepoint t=0. The final clathrin fluorescence intensities represents a clathrin fluorescence intensity after 30 minutes of assembly. Final graphs were generated with Origin 2024b v10.1.5.132.

Protein diffusion measurements

Protein coat diffusion after the recruitment was measured by using the Fluorescence Recovery After Photobleaching (FRAP) approach using an Olympus IX83 TIRF microscope as above. SLBs were incubated with desired concentrations of labeled HRS, and the protein recruitment was followed over time until the fluorescence intensity plateaued. The remaining bulk protein was then washed out with five consecutive washes with the reaction buffer. The diffusion of the membrane-bound protein was measured immediately by FRAP. A small region of protein on the membrane was photobleached, and the recovery of fluorescence was monitored by time-lapse imaging. Data was analyzed with Fiji v1.54f. First, the fluorescence intensity of the bleached region and the region outside the bleaching area was measured. Unwanted bleaching during imaging was then corrected by dividing the fluorescence value inside the bleached region by the value outside the bleached region. Finally, all values were subtracted from a background and then divided by the initial fluorescence value before photobleaching. Final curves were generated with Origin 2024b v10.1.5.132.

Platinum replica electron microscopy (PREM)

ARTICLE IN PRESS

For PREM samples, we prepared membrane-coated silica beads as described above. Round glass coverslips were plasma-cleaned and attached to a round metal, homemade sample holder to create a sample chamber. Membrane-coated silica beads were then hydrated in the reaction buffer (20mM HEPES pH 7.2, 125 mM KAc, 1 mM MgAc) until the SLB covered the glass surface. Exposed glass was then passivated with 2 mg/ml BSA solution. In between each protein addition, samples were washed five times with the reaction buffer. After the assembly of HRS and clathrin, samples were washed five times with a reaction buffer and then fixed with 2% glutaraldehyde/2% formaldehyde solution for 30 minutes. Samples were stored in 2 % glutaraldehyde in reaction buffer for 16-40 hours until the PREM replicas were prepared. SLBs were then sequentially treated with 0.5% OsO_4, 1% tannic acid, and 1% uranyl acetate before graded ethanol dehydration and hexamethyldisilane substitution (Sigma-Aldrich). Dried samples were rotary-shadowed with 2 nm of platinum and 6 nm of carbon using a high vacuum sputter coater (Leica Microsystems). The resultant platinum replica was floated off the glass with hydrofluoric acid (5%), washed several times with distilled water, and picked up on 200 mesh formvar/carbon-coated EM grids. Replicas on EM grids were mounted in a eucentric side-entry goniometer stage of either a transmission electron microscope operated at 80 kV (model CM120; Philips) equipped with a Morada digital camera (Olympus) or a transmission electron microscope running at 120 kV (Jeol) equipped with a Xarosa digital camera (EMSYS GmbH). Images were adjusted for brightness and contrast in Adobe Photoshop (Adobe) and presented in inverted contrast. Flat and curved clathrin coats were classified based on electron opacity analysis as described previously [85,86]. Clathrin-coated regions were manually delineated on PREM images using ImageJ and classified as either (i) flat clathrin lattices or (ii) curved clathrin pits. The classification was based on differences in electron beam transmission: flat lattices exhibited higher transmission consistent with a single membrane layer, whereas curved pits showed reduced transmission and increased apparent electron opacity due to the presence of multiple membrane layers. For each image, total membrane area was measured, and the surface area occupied by each clathrin category was quantified and expressed as a percentage of the total membrane area.

Quantification of multilayered clathrin coats

After acquiring images, they were processed with ImageJ software to adjust brightness and contrast, ensuring that electron opacity is visible and quantifiable. To quantify the density of clathrin layers, line profiles were drawn across regions of interest on various clathrin layers in the PREM images. ImageJ was then used to analyze these line profiles, allowing for precise quantification of the gray values that

ARTICLE IN PRESS

correspond to electron opacity or intensity. The analysis differentiates between various clathrin layers based on their line profiles by identifying distinct maxima and background levels. For instance, monolayer and double clathrin layers are characterized by two distinct maxima in their line profiles, with gray values that exceed the background levels. A gray value above the background level serves as a criterion to confirm the presence of an additional clathrin layer.

Fast Atomic force microscopy and Quantitative imaging

AFM images were acquired using a JPK NanoWizard Ultraspeed AFM (Bruker and JPK BioAFM) equipped with USC-F0.3-k0.3-10 cantilevers (Nanoworld) with a spring constant of 0.3 N/m and a resonance frequency of approximately 300 kHz. The Fast-AFM was operated in tapping mode, with the cantilever oscillating at a frequency close to 150 kHz.

Large unilamellar vesicles (LUVs) composed of DOPC:DOPS:DOPE:PI(3)P:Ch (29:20:20:1:30) were spread onto freshly cleaved mica surfaces to form supported lipid bilayers (SLBs) using buffer extension (10 mM HEPES, 2 mM $MgCl_2$, 10 mM $CaCl_2$, pH 7.4) at 37°C for 30 minutes. The samples were then gently rinsed three times with reaction buffer to remove excess non-bound lipids. SLBs were imaged before selecting and scanning the areas of interest (AOIs).

During imaging, HRS and clathrin samples were injected into the imaging chamber at final concentrations of 500 nM and 200 nM, respectively. First, the dynamics and mechanics of HRS were measured for at least 30 minutes using Fast-AFM imaging and quantitative Imaging (QI) mode, followed by clathrin injection and subsequent measurement. To minimize lateral frictional forces during clathrin injection and its interaction with HRS, QI mode was used. This mode provides quantitative nanomechanical data maps correlated with topography. A low force regime of 600–6800 pN was applied. The vertical length and forward velocity parameters were set to 100-250 nm and 50-120 μm/s depending on the topology height of the scanned area, respectively. Images were analyzed using JPKSPM Data Processing, Fiji, and WSxM software [87]. ROI areas of membranes on Mica were identified using the threshold plugin tool in Fiji. The height of membranes areas was then measured and set it as 0 nm. The protein coat thicknesses were measured by using threshold-identified membrane areas. The membrane surface height was subtracted from the final protein coat thickness.

Cell lines

HeLa MZ wild type and NPC1 knockout cell lines were a kind gift from Stefania Vossio (ACCESS, University of Geneva) [49]. HeLa Kyoto cell line constitutively expressing mCherry-HRS was a kind gift

ARTICLE IN PRESS

from Harald Stenmark (Faculty of Medicine, University of Oslo). We maintained these cells in high-glucose DMEM + GlutaMax-I (# 61965-026, Thermo Fisher Scientific) supplemented with penicillin-streptomycin solution (# 15140122, Thermo Fisher Scientific), 10% fetal bovine serum (# 10270-106, Thermo Fisher Scientific) and 1 mM sodium pyruvate (# 11390070 Thermo Fisher Scientific) in 37°C and 5% CO_2 cell culture incubator.

Live cell imaging

HeLa MZ cells were cultured as above on poly-D-lysine coated glass-bottom dishes. 16-24 hours later, cells were transfected with pcDNA3.1-GFP-HRS plasmids using Lipofectamine 3000 reagent (Thermo Fisher Scientific). 16 hours later culture media was changed to FluoroBrite DMEM (Gibco) supplemented with 10% FBS and penicillin-streptomycin solution. Cells were imaged with a DeltaVision Ultra microscope (Image Solution) equipped with Pco edge 4.2ge sCMOS camera and 60x 1.42 NA Oil objective. Acquisition for done with softWoRx-DV-AcquireUltra-1.2.3-RC1x86_64 software (Cytiva). To label endosomes, cells were treated with AlexaFluor 647 labelled EGF (# E35351, Thermo Fisher Scientific) for two minutes in normal culture media. Cells were then washed twice with warm FluoroBrite DMEM media and subsequently incubated for 15 minutes in a +37°C cell culture incubator to allow EGF trafficking to endosomes. Cells were then imaged immediately as described above. FRAP experiments of protein condensates in HeLa cells were performed with an Olympus IX83 microscope equipped with ImageEM X2 EM-CCD camera (Hamamatsu), Olympus Uapo N 60x NA 1.45 objective. Cytoplasmic GFP-HRS condensates were photobleached with the same microscope setup and data was analysed as described above.

CRISPR-Cas9 knock-in cell lines

We generated the mScarlet-I3-HRS (Supplementary Fig 2a) cell line by targeting the N-terminal part of the HRS genomic locus (ID 9146) with the guide RNA: 5' – GGTGCCGCTGCCTCGCCCCATGG-3' [Protospacer Adjacent Motif Sequence (PAM) is underlined] located at the start codon in the HRS coding sequence (PAM just before start codon). The designed guide RNA was purchased from Genescript. The guide RNA was designed using Benchling (https://www.benchling.com) and double-checked using the CRISPR-Cas9 guide RNA design checker from IDT (https://www.eu.idtdna.com/site/order/designtool/index) to analyze on-target and off-target score. For this guide RNA, no significant off-targets were detected. The Homology Repair (HR) primers (sense and anti-sense) were designed to be adjacent to the start codon from the

ARTICLE IN PRESS

genomic sequence and with a length of 55 nucleotides each. The primers used for HR templates were: Forward and HRS-Right-Homology-Arm sense: 5'-GCGCCCGCGGCGTCGGGTTTGGGCTGGAGGTCGCCATGGATAGCACCGAGGCCGT-3'; Reverse and HRS-Left-Homology-Arm anti-sense: 5'-AGACCACCTCCTCCTAGATCGTACCCCGCTCCGTCG CCGTGGAAGCTCGCAGAGGA-3'. The DNA sequence of the right and left homology arms was 35 nucleotides, and the sequence to hybridize with the fluorescent tag was 20 nucleotides. The primers were synthesized by Microsynth AG. The fluorescent tag mScarlet-I3 was synthesized *de novo* by Genescript. This fragment was cloned into a pUC57 plasmid using EcoRI and BamHI restriction enzymes. For the generation of mScarlet-I3, the amino acid sequence was obtained from FPbase (https://www.fpbase.org), and then, by using Genescript and Benchling algorithms, the optimized DNA codon sequence was obtained for best mammalian expression. To the 3'-terminus of mScarlet-I3, a long flexible linker (69 amino acids) was added to keep the maximum functionality of the tagged protein. This linker is designed to have multiple GS-rich regions, two times the ALFA epitope (5'- CCCAGCAGACTGGAAGAGGAAC TGCGGCGGAGACT GACAGAA -3') for Western Blott detection of the inserted tag, and a TEV cleavage site (5'-GAGAACCTGTACTTTCA AGGCGCCGCTAAGTTC-3') for downstream protein purification. The following double-strand DNA fragment was inserted into the pUC57 plasmid:

mScarlet-I3-GS-2xALFA-GS-TEV-GS: 5'-

ATGGATAGCACCGAGGCCGTGATCAAAGAGTTCATGCGGTTCAAGGTGCACATGGA
AGGCAGCATGAACGGCCACGAGTTCGAGATCGAAGGCGAAGGCGAGGGCAGACCTT
ATGAGGGAACACAGACCGCCAAGCTGAAAGTGACCAAAGGCGGCCCTCTGCCTTTCA
GCTGGGACATTCTGAGCCCTCAGTTTATGTACGGCAGCCGGGCCTTCATCAAGCACC
CTGCCGATATTCCCGACTACTGGAAGCAGAGCTTCCCCGAGGGCTTCAAGTGGGAGA
GAGTGATGATCTTCGAGGACGGCGGCACCGTGTCTGTGACCCAGGATACAAGCCTG
GAAGATGGCACCCTGATCTACAAAGTGAAGCTGAGAGGCGGCAACTTCCCTCCTGAT
GGCCCCGTGATGCAGAAAAGAACCATGGGCTGGGAAGCCAGCACCGAGAGACTGTA
CCCTGAGGACGTGGTGCTGAAGGGCGACATCAAGATGGCCCTGAGACTGAAGGATG
GCGGCAGATACCTGGCCGACTTCAAGACCACCTACAAGGCCAAGAAACCCGTGCAGA
TGCCAGGCGCCTTCAACATCGACCGGAAGCTGGATATCACCAGCCACAACGAGGACT
ACACCGTGGTGGAACAGTACGAGAGAAGCGTGGCCAGACACAGCACAGGTGGAAGC

ARTICLE IN PRESS

GGAGGATCTTCCTCAACTGGTGGTGGAGGTTCTAGTCCCAGCAGACTGGAAGAGGA
ACTGCGGCGGAGACTGACAGAAGGCGGCGGAGGATCTTCTGGCCCTTCTGGATCTA
GCAGCCCCTCCAGGCTGGAGGAAGAACTGAGAAGAAGGCTGACCGAGGAGAACCTG
TACTTTCAAGGCGCCGCTAAGTTCAGCTCTGGTGGAGGAGGATCTAGC -3'.

For the generation of the double-strand DNA Donor Template, we produced PCR cassettes using the plasmid generated before together with the HR Right-Left primers to amplify the tag with the 35 nucleotide-Homology Arms. For the PCR amplification, the PrimeSTAR Max DNA Polymerase kit (#R045A) from Takara was used. For the purification of the PCR product, the QIAquick PCR and gel Cleanup kit (28506) from Qiagen was used. HeLa MZ cells were seeded into a 24-well plate at $1x10^5$ cells/mL without antibiotics one day before transfection. We used the Lipofectamine CRISPRMAX Cas9 (CMAX00008) as a Transfection Reagent from Thermofisher, and we followed the manufacturer's indications for the transfection. Together with the transfection system, we used the purified GenCrispr NLS-Cas9-EGFP Nuclease (Z03467) from Genescript, the guide RNA designed to target HRS, and the HR PCR cassettes generated as a template (500 ng/well). Just before adding the Cas9/gRNA complex, the media was replaced with new media without antibiotics, and Alt-R HDR Enhancer V2 (10007921) from Integrated DNA Technologies to increase the chances of Homology-Directed Repair events after the DNA double-strand break by the Cas9 nuclease. One day later, the media was replaced for new media with antibiotics. To obtain single-cell clones of mScarlet-I3-HRS Knock-In, cells were subjected to FACS, and single cells were deposited in a well of a 96-well plate. For the validation of the cell lines, clones were genotyped via Western Blot using anti-HRS and anti-ALFA antibodies (see Supplementary Table 4), fluorescent microscopy, and PCR using the following primers: HRS Forward 5'-GTTCTTAGGGCTCATTGTTCCA-3' targeting the 5'-UTR, and therefore, before the start codon; and HRS Reverse 5'-AGTTCACTCTGTGGAAGGAACG-3' targeting the HRS coding sequence after the start codon. For the genomic DNA extraction, the QIAamp DNA Mini kit (51304) from Qiagen was used. Final validation was performed, followed by sequencing PCR amplified regions to check the correct insertion of the tag using Microsynth AG sequencing service. The HeLa MZ with endogenous Scarlet-I3-HRS cell line is available upon request from the corresponding author.

Western blot

An identical number of cells from each cell lines were cultured on 6-well plates. 16-24 hours later, cells were washed twice with PBS and then 1x Laemmli sample buffer was added on cells and cells were

ARTICLE IN PRESS

detached with a scraper. Samples were then boiled for 5 minutes and spinned down. Identical amount of samples were loaded on 4-20% gradient SDS-PAGE gels (Biorad). After SDS-PAGE run, protein was transferred to nitrocellulose membranes and membranes were subsequently blocked with 5% BSA in PBS. Primary antibodies (Supplementary table 4) were diluted in 5% BSA and incubated on membranes with agitation overnight in +4°C. Membranes were then washed five times with PBS supplemented with 0.05% (w/v) Tween-20. Secondary HRP-conjugated antibodies were then incubated on membranes under agitation for one hour at room temperature. After washing as above, membranes were incubated for two minutes with ECL solution before detection. Protein expression levels were quantified with Fiji v1.54f.

Western blot analysis revealed that one of the clonal cell lines was heterozygous for HRS-mScarlet-I3, while the other one was homozygous for HRS-mScarlet-I3. We noted that tagging of HRS decreased its expression levels (Supplementary Fig 2b,g).

Epidermal growth factor (EGF) pulse-chase

We performed the EGF pulse-chase experiment as described in [18]. Shortly, HeLa mScarlet-I3-HRS cells were cultured on Poly-D-lysine coated coverslips, and 50 ng/ml AlexaFluor-647 EGF (# E35351, Thermo Fisher Scientific) in normal cell culture media was incubated with cells for 2 minutes in +37°C. Cells were then washed twice with normal cell culture media and incubated for 5, 15, 30, and 45 minutes in normal cell culture media at 37°C before fixation with 4% formaldehyde solution in PBS. Cells were then washed three times with PBS before coverslips were mounted on microscope slides as described above. Cells were imaged with Stellaris 8 Falcon (Leica) confocal microscope equipped with Lightning using a 60x oil objective. Acquisition for done with LAS X version 4.9.0.30221 (Leica Microsystems). Colocalization of AlexaFluor-646 EGF with mScarlet-I3-HRS was analyzed with Fiji v1.54f using BIOP JaCoP plugin (https://github.com/BIOP/ijp-jacop-b). Final graphs were generated with Origin 2024b v10.1.5.132.

Cryo-CLEM and cryo-ET

HeLa MZ cells with endogenous HRS tagged with Scarlet-I3-HRS and HeLa Kyoto cells stably expressing HRS-mCherry [18,19] were grown on 200 mesh gold EM grids with a holey carbon film R2/2 (Quantifoil). Cells were incubated with 50 ng/ml EGF-Alexa 647. After allowing internalization of the cargo for 15 minutes at 37°C, the remaining EGF-Alexa647 was washed away with cell culture media. The EM grids were backside-blotted for 12 seconds using Whatman No.1 filter paper and

ARTICLE IN PRESS

vitrified using a manual plunger with a cryostat [88] between 7 and 12 minutes after the removal of EGF-Alexa647.

Thin lamellae of the cells were obtained by cryo-focused ion beam milling in an Aquilos 2 cryo-FIB-SEM (Thermo Fisher Scientific), equipped with an integrated fluorescence light microscope (iFLM). Grids were subjected to platinum coating for 1 minute and 30 seconds. Lamellae were prepared using standard semi-automated protocols [89,90]. Eucentricity, finding milling angles, stress relief cuts, and rough and medium milling steps were performed using the Cryo AutoTEM software in an automatic manner (Thermo Fisher Scientific). After assessing rough-milled lamella for signals of interest by iFLM, final polishing to a target thickness of 200-250 nm was performed manually. In some cases, the final lamellae were again imaged by iFLM to identify regions for cryo-ET acquisition. The grids with the lamellae were then transferred to a Krios G4 C-FEG cryo-TEM operated at 300 kV for cryo-EM and cryo-ET imaging. Z-stacks acquired by iFLM were correlated to cryo-EM overview maps to target regions containing HRS or EGF signals by cryo-ET. We thereby obtained 5 tomograms with EGF-Alexa647, and 6 tomograms with mScarlet-I3-HRS signals. In one additional tomogram, an EGF-Alexa647 signal was too weak to unambiguously identify, yet the coat was visible. In two of the mScarlet-I3-HRS tomograms, the coat was not identifiable, possibly due to the oblique orientation of membranes relative to the imaging plane. The final data set thus consisted of 10 tomograms, some containing multiple endosomes with visible coat (Figures 6a-c and Supplementary Fig 7e-p).

Cryo-EM and ET data was acquired on a Krios G4 C-FEG equipped with a Falcon 4 detector used in counting mode and a Selectris energy filter. Data was collected with Tomography 5 Software (Thermo Fisher Scientific). Lamellae maps were acquired at a defocus of -60 µm and a pixel size of 53.7 Å. Tilt series were acquired with a dose-symmetric tilt scheme [91] in groups of 4 between -60° and 60° at an increment of 1° and a pixel size of 2.97 Å. Some tilt series were not acquired at the full range between -60° and 60°. A dose of approximately 1 e-/Å^2 was applied per tilt angle. The target defocus was -5 µm. Tilt series alignment was performed with IMOD using patch tracking, and for figure presentation, tomograms were reconstructed by SIRT at bin 2 using IMOD [92,93]. A 3D median filter was applied to the reconstructed tomograms for figure presentation.

Subtomogram averaging

ARTICLE IN PRESS

For subtomogram averaging, tomograms were reconstructed by weighted back projection after CTF-correcting tilt series using phase flipping in IMOD [92,93]. Of the 12 tomograms with the visible coat, we used 8 for further processing (Supplementary Table 3).

Subtomogram averaging was performed using Dynamo [94]. Initially, coat-containing membranes were manually annotated using the surface model of Dynamo Catalogue [95] and 1809 segments were extracted on the hard drive. For the initial alignment, a subset of 50 particles was manually coarsely aligned using **dynamo_gallery**. These particles underwent an initial alignment process, and the resulting average was used as a reference for the global alignment of all subtomograms. Subsequent refinement steps involved iterative rounds of alignment and classification in Dynamo. Multireference alignment was performed to sort particles into the classes with the layers and the suboptimal classes. Particles from both good and bad classes were manually inspected in **dynamo_gallery** to recover misclassified particles. After several rounds of classification and manual inspection, 440 particles were identified as the final set and used for the subtomogram averaging. The final 3D map was first refined without symmetry constraints. Next, disc-like masks were tested for subtomogram averaging, allowing the particles to rotate only around the vertical axis and to shift in-plane. The alignment focused on the first layer resulted in an apparent hexametric lattice. To further enhance the structural details, C6 symmetry was applied in the final rounds of refinement, resulting in a final resolution of 44 Å (Supplementary Table 3). Similar focused refinements on the other layers did not reveal apparent symmetry.

ARTICLE IN PRESS

Immunofluorescence staining and imaging

For immunofluorescence microscopy, we cultured cells on Poly-D-Lysine (# A3890401, Thermo Fisher Scientific) coated coverslips, washed cells two times with PBS and then fixed them for 15 minutes in room temperature with 4% formaldehyde solution in PBS. Cells were washed three times with 0.2% saponin in PBS, then permeabilized and blocked with 3% BSA, 100 mM glycine, and 0.2% saponin in PBS for 1 hour and then incubated overnight with primary antibodies (see Supplementary Table 4 for dilutions) in 1% BSA, 0.2% saponin in PBS at +4°C. Cells were then washed three times with saponin-PBS solution and incubated for 1 hour at room temperature with secondary antibodies (Supplementary Table 4) in 1% BSA 0.2% saponin in PBS. Before mounting the coverslips on microscope slides with ProLong Glass Antifade Mountant (# P36982, Thermo Fisher Scientific), cells were washed two times with PBS and once with water. We imaged cells with a Stellaris 8 Falcon (Leica) confocal microscope equipped with Lightning using a 60x oil objective.

ARTICLE IN PRESS

Filipin staining for HeLa mScarlet-I3-HRS cells cultured on Poly-D-lysine coated coverslips was done after cells were fixed for 15 minutes with 4% formaldehyde in PBS. Cells were then washed three times with PBS, and 50 μg/ml Filipin (# F9765, Sigma-Aldrich) in PBS was incubated on cells for 30 minutes at room temperature. Samples were mounted on microscope slides with ProLong Glass Antifade Mountant, and samples were imaged during the same day with a Stellaris 8 Falcon (Leica) confocal microscope equipped with Lightning using a 60x oil objective.

High-content imaging

To modify cholesterol amounts in the endo-lysosomal pathway, cells were treated with U18666A (# 3633, Sigma-Aldrich) or Methyl-b-cyclodextrin (MbCD, # C4555, Sigma-Aldrich). For the U18666A treatment, cells were cultured on normal media. The following day, 3 μg/ml of U18666A in normal cell culture media was added to cells, and cells were cultured for 24 hours before they were fixed with 4% formaldehyde in PBS. Cholesterol amounts at the endo-lysosomal pathway were verified with Filipin staining.

For high-content imaging, cells were cultured in μ-Plate 96 well plates (# 89626, Ibidi GmbH) and immunostained as described above. Hoechts 33342 staining (1:10,000 dilution, # H3570, Thermo Fisher Scientific) was performed at the same time with a secondary antibody staining. Cells were imaged with ImageXpress Micro confocal microscope (Molecular Devices) equipped with an sCMOS camera. Cells were segmented and analyzed with MetaXpress (Molecular Devices). To segment nuclei and cells, we used Hoechst signal. To measure the intensity of HRS-positive clathrin, we first segmented images based on the HRS signal and then used this segmentation to measure clathrin fluorescence intensity in HRS-positive patches. HRS patch sizes were measured from the segmented HRS signals. Final graphs were generated with Origin 2024b v10.1.5.132.

Cholesterol clustering in large unilamellar vesicles (LUVs)

LUVs were prepared by mixing lipids at 1 mg/ml final concentration in chloroform with a composition of 29 mol% DOPC, 20 mol% DOPE, 20 mol% DOPS, 1 mol% PI(3)P, 29.5 mol% cholesterol, and 0.5 mol% TopFluor-cholesterol. Chloroform was evaporated under argon gas and then in a vacuum, and lipids were hydrated in a reaction buffer (20 mM HEPES pH 7.2, 125 mM KAc). Liposomes were then freeze-thawed 10 times with a water bath and liquid nitrogen and then extruded through 100-nm polycarbonate filters using a mini extruder (Avanti Polar Lipids). To measure TopFluor-cholesterol fluorescence quenching, the final concentration of 50 μM liposomes

ARTICLE IN PRESS

was mixed with the desired concentration of HRS in the reaction buffer. After 60 minutes, we measured TopFluor-cholesterol spectra between 490 nm and 550 nm with 2 nm steps using a BioTek Synergy H1 plate reader (Agilent Technologies). Final graphs were generated with Origin 2024b v10.1.5.132.

Cholesterol sorting and diffusion with SLBs

SLBs with lipid composition of 29 mol% DOPC, 20 mol% DOPE, 20 mol% DOPS, 1 mol& PI(3)P, 29 mol% cholesterol and 1 mol% TopFluor-cholesterol were prepared as above. HRS at μM concentration and clathrin at 200 nM concentration were incubated with SLBs as described above. We recorded TopFluor cholesterol sorting with a Nikon Eclipse C1 spinning disk confocal microscope using a 100x 1.3 NA objective. The microscope was controlled with Slidebook 6.0.22 (3i Intelligent Imaging Innovations), and the data analysis was performed using Fiji v1.54f. Final graphs were generated with Origin 2024b v10.1.5.132.

To measure TopFluor-cholesterol diffusion with fluorescence recovery after the photobleaching (FRAP) approach, we prepared samples with either 500 nM or 2 μM HRS and 200 nM clathrin, as described above. We performed FRAP experiments with an Olympus IX83 TIRF microscope equipped with ImageEM X2 EM-CCD camera (Hamamatsu) and FRAP laser, using Olympus Uapo N 100x NA 1.49 objective. The microscope was controlled with Visiview v.4.4.0.11 software (Visitron Systems). We imaged a timelapse series of SLBs with a 500 ns frame rate. Before bleaching the small region of SLB, we recorded 3-5 frames, and after bleaching, we recorded 1-2 minutes until the recovery plateaued. We analyzed the data with Fiji v1.54f. Final graphs were generated with Origin 2024b v10.1.5.132. FRAP immobile fractions and halftimes of mobile fractions were calculated with a one-phase exponential equation:

$$y = A1 \times e^{t/\tau} + y0$$

where A is the value of y in the plateau, t is time, τ is a time constant, and y0 is the value of y when t=0. Recovery halftimes were then calculated with the equation:

$$\text{halftime} = \tau \times ln(2)$$

Cargo protein reconstitution and clustering

ARTICLE IN PRESS

LUVs with and without cholesterol (29.9 mol% DOPC, 20 mol% DOPE, 20 mol% DOPS, 1 mol& PI(3)P, 30 mol% cholesterol and 0.1 mol% Atto647-DOPE and 69.9 mol% DOPC, 20 mol% DOPE, 20 mol% DOPS, 1 mol& PI(3)P, and 0.1 mol% Atto647-DOPE), respectively, were used to reconstitute SfGFP-VAMP2-4xUb produced recombinantly, as previously performed with other transmembrane proteins [96](Figure 6a). Briefly, LUVs were initially incubated in the presence of 0.1% Triton X100 for 30 minutes (Figure 6a, step 1). Detergent-destabilized liposomes were then mixed with purified protein at a protein:lipid molar ratio of 1:500. After 30 minutes of incubation at room temperature with gentle agitation, the Triton X100 detergent was removed using BioBeads SM-2 adsorbent (BioRad) by four consecutive additions to the proteo-lipid mixture every hour, followed by an overnight incubation [97]. The sample was then spin-down to remove the BioBeads and non-incorporated protein, and the supernatant containing the proteoliposomes was collected (Figure 6a, step 2).

To perform the GUVs with reconstituted protein, proteoliposomes were dialyzed against a 25 mM HEPES and 1 mM Trehalose solution for 2 hours. After dialysis, 15 µl of the freshly dialyzed sample was placed on a clean parafilm surface and mixed with 2 µl of 40 um silica beads (Microspheres-Nanospheres, USA), and then dried in a vacuum chamber for at least 1 hour (Figure 6a, step 3). The dried beads covered with the proteo-lipid layers were then transferred to a tube containing 10 µl of 1M Trehalose solution for 15 min at 65 °C. Next, the 10 µl containing the pre-hydrated proteo-lipid lamellas were transferred to the observation chamber containing the working buffer (20 mM HEPES, pH 7.2, 125 mM KAc, 1 mM MgAc) for complete proteo-GUVs hydration (Figure 6a, step 4). Lastly, mScarlet-I3-HRS at a final concentration of 400 nM was added to the microscopy chamber and incubated for 30 min before starting the imaging, using a spinning-disk Nikon Ti-Eclipse.

Statistics and reproducibility

All statistical analyses were performed with Origin 2024b v10.1.5.132. All data sets were tested for normality. For normally distributed data or data with a sample size (n) over 50, the statistical significance was tested with a two-tailed Welch's t-test. For non-normally distributed datasets, the statistical significance was tested with a Kruskal-Wallis test. All box plots in this work show median values as a solid line. Box indicates the 25th and 75th percentiles, and whiskers indicate the 5th and 95th percentiles. Individual data points are shown in all box plots. All in vitro reconstitution and cell biology data were successfully repeated at least three times. All PREM and AFM data were successfully repeated at least twice.

ARTICLE IN PRESS

Data availability

Source data are provided within the Source Data File. Fluorescence microscopy data are provided at FigShare image repository [doi: 10.6084/m9.figshare.30901727]. Original Western blot images are provided as supplementary data files. Subtomogram averages EMD-56110 [https://www.ebi.ac.uk/emdb/EMD-56110] and tomograms EMD-56112 [https://www.ebi.ac.uk/emdb/EMD-56112] are provided upon publication at the Electron Microscopy Data Bank (EMDB). All other data is available from the corresponding authors.

ARTICLE IN PRESS

References

1. Ybe, J. A. *et al.* Clathrin self-assembly is mediated by a tandemly repeated superhelix. *Nature* **399**, 371–375 (1999).
2. Liu, S.-H., Wong, M. L., Craik, C. S. & Brodsky, F. M. Regulation of clathrin assembly and trimerization defined using recombinant triskelion hubs. *Cell* **83**, 257–267 (1995).
3. Roth, T. F. & Porter, K. R. Yolk protein uptake in the oocyte of the mosquito Aedes aegypti L. *J. Cell Biol.* **20**, 313–332 (1964).
4. Ungewickell, E. & Branton, D. Assembly units of clathrin coats. *Nature* **289**, 420–422 (1981).
5. Crowther, R. A. & Pearse, B. M. Assembly and packing of clathrin into coats. *J. Cell. Biol.* **91**, 790–797 (1981).
6. Kaksonen, M. & Roux, A. Mechanisms of clathrin-mediated endocytosis. *Nat. Rev. Mol. Cell Biol.* **19**, 313–326 (2018).
7. Sochacki, K. A. & Taraska, J. W. From Flat to Curved Clathrin: Controlling a Plastic Ratchet. *Trends Cell Biol.* **29**, 241–256 (2019).

ARTICLE IN PRESS

8. Vassilopoulos, S. & Montagnac, G. Clathrin assemblies at a glance. *J. Cell Sci.* **137**, jcs261674 (2024).

9. Lock, J. G. *et al.* Clathrin-containing adhesion complexes. *J. Cell Biol.* **218**, 2086–2095 (2019).

10. Hakanpää, L. *et al.* Reticular adhesions are assembled at flat clathrin lattices and opposed by active integrin α5β1. *J. Cell Biol.* **222**, e202303107 (2023).

11. Elkhatib, N. *et al.* Tubular clathrin/AP-2 lattices pinch collagen fibers to support 3D cell migration. *Science* **356**, eaal4713 (2017).

12. Raiborg, C., Bache, K. G., Mehlum, A., Stang, E. & Stenmark, H. Hrs recruits clathrin to early endosomes. *EMBO J.* **20**, 5008–5021 (2001).

13. Sachse, M., Urbé, S., Oorschot, V., Strous, G. J. & Klumperman, J. Bilayered Clathrin Coats on Endosomal Vacuoles Are Involved in Protein Sorting toward Lysosomes. *Mol. Biol. Cell* **13**, 1313–1328 (2002).

14. Raiborg, C. *et al.* FYVE and coiled-coil domains determine the specific localisation of Hrs to early endosomes. *J. Cell Sci.* **114**, 2255–2263 (2001).

15. Prag, G. *et al.* The Vps27/Hse1 Complex Is a GAT Domain-Based Scaffold for Ubiquitin-Dependent Sorting. *Developmental Cell* **12**, 973–986 (2007).

16. Ren, X. *et al.* Hybrid Structural Model of the Complete Human ESCRT-0 Complex. *Structure* **17**, 406–416 (2009).

17. Raiborg, C. *et al.* Hrs sorts ubiquitinated proteins into clathrin-coated microdomains of early endosomes. *Nat. Cell Biol.* **4**, 394–398 (2002).

18. Wenzel, E. M. *et al.* Concerted ESCRT and clathrin recruitment waves define the timing and morphology of intraluminal vesicle formation. *Nat. Commun.* **9**, (2018).

ARTICLE IN PRESS

ARTICLE IN PRESS

19. Migliano, S. M. *et al.* Removal of hypersignaling endosomes by simaphagy. *Autophagy* 1–23 (2023) doi:10.1080/15548627.2023.2267958.

20. Kim, Y. & Burd, C. G. Lipid Sorting and Organelle Identity. *Cold Spring Harb. Perspect. Biol.* **15**, a041397 (2023).

21. Bigay, J. & Antonny, B. Curvature, Lipid Packing, and Electrostatics of Membrane Organelles: Defining Cellular Territories in Determining Specificity. *Dev. Cell* **23**, 886–895 (2012).

22. Anderson, R. H. *et al.* Sterols lower energetic barriers of membrane bending and fission necessary for efficient clathrin-mediated endocytosis. *Cell Rep.* **37**, 110008 (2021).

23. Rodal, S. K. *et al.* Extraction of cholesterol with methyl-beta-cyclodextrin perturbs formation of clathrin-coated endocytic vesicles. *Mol. Biol. Cell* **10**, 961–74 (1999).

24. Pichler, H. & Riezman, H. Where sterols are required for endocytosis. *Biochim. Biophys. Acta - Biomembr.* **1666**, 51–61 (2004).

25. Van Meer, G., Voelker, D. R. & Feigenson, G. W. Membrane lipids: where they are and how they behave. *Nat. Rev. Mol. Cell Biol.* **9**, 112–124 (2008).

26. Ikonen, E. Mechanisms of cellular cholesterol compartmentalization: recent insights. *Curr. Opin. Cell Biol.* **53**, 77–83 (2018).

27. Wheeler, S. & Sillence, D. J. Niemann–Pick type C disease: cellular pathology and pharmacotherapy. *J. Neurochem.* **153**, 674–692 (2020).

28. Ikonen, E. & Zhou, X. Cholesterol transport between cellular membranes: A balancing act between interconnected lipid fluxes. *Dev. Cell* **56**, 1430–1436 (2021).

29. Carstea, E. D. *et al.* Niemann-Pick C1 Disease Gene: Homology to Mediators of Cholesterol Homeostasis. *Science* **277**, 228–231 (1997).

ARTICLE IN PRESS

ARTICLE IN PRESS

30. Naureckiene, S. *et al.* Identification of HE1 as the Second Gene of Niemann-Pick C Disease. *Science* **290**, 2298–2301 (2000).

31. Gillooly, D. J. Localization of phosphatidylinositol 3-phosphate in yeast and mammalian cells. *EMBO J.* **19**, 4577–4588 (2000).

32. Urbé, S., Mills, I. G., Stenmark, H., Kitamura, N. & Clague, M. J. Endosomal localization and receptor dynamics determine tyrosine phosphorylation of hepatocyte growth factor-regulated tyrosine kinase substrate. *Mol Cell Biol* **20**, 7685–7692 (2000).

33. Banani, S. F., Lee, H. O., Hyman, A. A. & Rosen, M. K. Biomolecular condensates: organizers of cellular biochemistry. *Nat Rev Mol Cell Biol* **18**, 285–298 (2017).

34. Lyu, X. *et al.* A gel-like condensation of Cidec generates lipid-permeable plates for lipid droplet fusion. *Dev. Cell* **56**, 2592-2606.e7 (2021).

35. Snead, W. T. & Gladfelter, A. S. The Control Centers of Biomolecular Phase Separation: How Membrane Surfaces, PTMs, and Active Processes Regulate Condensation. *Mol. Cell* **76**, 295–305 (2019).

36. Zhao, X., Bartolucci, G., Honigmann, A., Jülicher, F. & Weber, C. A. Thermodynamics of wetting, prewetting and surface phase transitions with surface binding. *New J. Phys.* **23**, 123003 (2021).

37. Abramson, J. *et al.* Accurate structure prediction of biomolecular interactions with AlphaFold 3. *Nature* **630**, 493–500 (2024).

38. Erdős, G., Pajkos, M. & Dosztányi, Z. IUPred3: prediction of protein disorder enhanced with unambiguous experimental annotation and visualization of evolutionary conservation. *Nucleic Acids Research* **49**, W297–W303 (2021).

ARTICLE IN PRESS

ARTICLE IN PRESS

39. Hardenberg, M., Horvath, A., Ambrus, V., Fuxreiter, M. & Vendruscolo, M. Widespread occurrence of the droplet state of proteins in the human proteome. *Proc. Natl. Acad. Sci. U.S.A.* **117**, 33254–33262 (2020).

40. Liang, Q. *et al.* MolPhase, an advanced prediction algorithm for protein phase separation. *EMBO J* **43**, 1898–1918 (2024).

41. Wilson, C., Lewis, K. A., Fitzkee, N. C., Hough, L. E. & Whitten, S. T. ParSe 2.0: A web tool to identify drivers of protein phase separation at the proteome level. *Protein Science* **32**, e4756 (2023).

42. Heuser, J. Three-dimensional visualization of coated vesicle formation in fibroblasts. *J. Cell Biol* **84**, 560–583 (1980).

43. Wernert, F. *et al.* The actin-spectrin submembrane scaffold restricts endocytosis along proximal axons. *Science* **385**, eado2032 (2024).

44. Sochacki, K. A., Dickey, A. M., Strub, M. P. & Taraska, J. W. Endocytic proteins are partitioned at the edge of the clathrin lattice in mammalian cells. *Nat. Cell Biol.* **19**, 352–361 (2017).

45. Sochacki, K. A. *et al.* The structure and spontaneous curvature of clathrin lattices at the plasma membrane. *Dev. Cell* **56**, 1131-1146.e3 (2021).

46. Fotin, A. *et al.* Molecular model for a complete clathrin lattice from electron cryomicroscopy. *Nature* **432**, 573–579 (2004).

47. Kravčenko, U. *et al.* Molecular architecture of synaptic vesicles. *Proc. Natl. Acad. Sci. U.S.A.* **121**, e2407375121 (2024).

48. Raiborg, C., Wesche, J., Malerød, L. & Stenmark, H. Flat clathrin coats on endosomes mediate degradative protein sorting by scaffolding Hrs in dynamic microdomains. *J. Cell Sci.* **119**, 2414–2424 (2006).

ARTICLE IN PRESS

ARTICLE IN PRESS

49. Vacca, F. *et al.* Cyclodextrin triggers MCOLN1-dependent endo-lysosome secretion in Niemann-Pick type C cells. *J. Lipid Res.* **60**, 832–843 (2019).

50. Pentchev, P. G. *et al.* A defect in cholesterol esterification in Niemann-Pick disease (type C) patients. *Proc. Natl. Acad. Sci. U.S.A.* **82**, 8247–8251 (1985).

51. Liscum, L., Ruggiero, R. M. & Faust, J. R. The intracellular transport of low density lipoprotein-derived cholesterol is defective in Niemann-Pick type C fibroblasts. *J. Cell Biol.* **108**, 1625–1636 (1989).

52. Liscum, L. & Faust, J. R. The intracellular transport of low density lipoprotein-derived cholesterol is inhibited in Chinese hamster ovary cells cultured with 3-β-[2-(diethylamino)ethoxy]androst-5-en-17-one. *J. Biol. Chem* **264**, 11796–11806 (1989).

53. Saleem, M. *et al.* A balance between membrane elasticity and polymerization energy sets the shape of spherical clathrin coats. *Nat. Commun.* **6**, e6249 (2015).

54. Chiaruttini, N. *et al.* Relaxation of Loaded ESCRT-III Spiral Springs Drives Membrane Deformation. *Cell* **163**, 866–879 (2015).

55. Souza, D. P. *et al.* Asgard archaea reveal the conserved principles of ESCRT-III membrane remodeling. *Sci. Adv.* **11**, eads5255 (2025).

56. Zhao, H. & Lappalainen, P. A simple guide to biochemical approaches for analyzing protein-lipid interactions. *Mol. Biol. Cell* **23**, 2823–2830 (2012).

57. Kefauver, J. M. *et al.* Cryo-EM architecture of a near-native stretch-sensitive membrane microdomain. *Nature* **632**, 664–671 (2024).

58. Banjade, S., Zhu, L., Jorgensen, J. R., Suzuki, S. W. & Emr, S. D. Recruitment and organization of ESCRT-0 and ubiquitinated cargo via condensation. *Sci. Adv.* **8**, eabm5149 (2022).

ARTICLE IN PRESS

ARTICLE IN PRESS

59. Takahashi, H., Mayers, J. R., Wang, L., Edwardson, J. M. & Audhya, A. Hrs and STAM Function Synergistically to Bind Ubiquitin-Modified Cargoes In Vitro. *Biophys. J.* **108**, 76–84 (2015).

60. Dannhauser, P. N. & Ungewickell, E. J. Reconstitution of clathrin-coated bud and vesicle formation with minimal components. *Nat. Cell Biol.* **14**, 634–639 (2012).

61. Kovtun, O., Dickson, V. K., Kelly, B. T., Owen, D. J. & Briggs, J. A. G. Architecture of the AP2/clathrin coat on the membranes of clathrin-coated vesicles. *Sci. Adv.* **6**, eaba8381 (2020).

62. Avinoam, O., Schorb, M., Beese, C. J., Briggs, J. A. G. & Kaksonen, M. Endocytic sites mature by continuous bending and remodeling of the clathrin coat. *Science* **348**, 1369–1372 (2015).

63. van Niel, G. *et al.* The Tetraspanin CD63 Regulates ESCRT-Independent and -Dependent Endosomal Sorting during Melanogenesis. *Dev. Cell* **21**, 708–721 (2011).

64. Raposo, G., Tenza, D., Murphy, D. M., Berson, J. F. & Marks, M. S. Distinct Protein Sorting and Localization to Premelanosomes, Melanosomes, and Lysosomes in Pigmented Melanocytic Cells✪. *The Journal of Cell Biology* **152**, 809–824 (2001).

65. Tagiltsev, G., Haselwandter, C. A. & Scheuring, S. Nanodissected elastically loaded clathrin lattices relax to increased curvature. *Sci. Adv.* **7**, eabg9934 (2021).

66. Ravindran, R. & Michnick, S. W. Biomolecular condensates as drivers of membrane trafficking and remodelling. *Curr. Opin. Cell Biol.* **89**, 102393 (2024).

67. Yuan, F. *et al.* Membrane bending by protein phase separation. *Proc. Natl. Acad. Sci. U.S.A.* **118**, e2017435118 (2021).

68. Mangiarotti, A., Chen, N., Zhao, Z., Lipowsky, R. & Dimova, R. Wetting and complex remodeling of membranes by biomolecular condensates. *Nat. Commun.* **14**, 2809 (2023).

ARTICLE IN PRESS

ARTICLE IN PRESS

69. Bussi, C. *et al.* Stress granules plug and stabilize damaged endolysosomal membranes. *Nature* **623**, 1062–1069 (2023).

70. Schiano Lomoriello, I., Sigismund, S. & Day, K. J. Biophysics of endocytic vesicle formation: A focus on liquid–liquid phase separation. *Curr. Opin. Cell Biol.* **75**, 102068 (2022).

71. Kozak, M. & Kaksonen, M. Condensation of Ede1 promotes the initiation of endocytosis. *eLife* **11**, e72865 (2022).

72. Day, K. J. *et al.* Liquid-like protein interactions catalyse assembly of endocytic vesicles. *Nat. Cell Biol.* **23**, 366–376 (2021).

73. Dragwidge, J. M. *et al.* Biomolecular condensation orchestrates clathrin-mediated endocytosis in plants. *Nat Cell Biol* **26**, 438–449 (2024).

74. Lolicato, F. *et al.* Cholesterol promotes clustering of PI(4,5)P2 driving unconventional secretion of FGF2. *J. Cell Biol.* **221**, e202106123 (2022).

75. Wang, H.-Y. *et al.* Coupling of protein condensates to ordered lipid domains determines functional membrane organization. *Sci. Adv.* **9**, eadf6205 (2023).

76. Norris, A. *et al.* SNX-1 and RME-8 oppose the assembly of HGRS-1/ESCRT-0 degradative microdomains on endosomes. *Proc. Natl. Acad. Sci. U.S.A.* **114**, E307–E316 (2017).

77. Palmulli, R. *et al.* CD63 sorts cholesterol into endosomes for storage and distribution via exosomes. *Nat. Cell Biol.* https://doi.org/10.1038/s41556-024-01432-9 (2024) doi:10.1038/s41556-024-01432-9.

78. Meng, Y., Heybrock, S., Neculai, D. & Saftig, P. Cholesterol Handling in Lysosomes and Beyond. *Trends Cell Biol.* **30**, 452–466 (2020).

ARTICLE IN PRESS

ARTICLE IN PRESS

79. Ikonen, E. Cellular cholesterol trafficking and compartmentalization. *Nat. Rev. Mol. Cell Biol.* **9**, 125–138 (2008).

80. Subtil, A. *et al.* Acute cholesterol depletion inhibits clathrin-coated pit budding. *Proc. Natl. Acad. Sci. U.S.A.* **96**, 6775–6780 (1999).

81. Scholz, J., Besir, H., Strasser, C. & Suppmann, S. A new method to customize protein expression vectors for fast, efficient and background free parallel cloning. *BMC biotechnology* **13**, 12 (2013).

82. Ahle, S. & Ungewickell, E. Purification and properties of a new clathrin assembly protein. *EMBO J* **5**, 3143–3149 (1986).

83. Weinberger, A. *et al.* Gel-assisted formation of giant unilamellar vesicles. *Biophys. J.* **105**, 154–164 (2013).

84. Brodsky, F. M. Living with Clathrin: Its Role in Intracellular Membrane Traffic. *Science* **242**, 1396–1402 (1988).

85. Moulay, G. *et al.* Alternative splicing of clathrin heavy chain contributes to the switch from coated pits to plaques. *Journal of Cell Biology* **219**, e201912061 (2020).

86. Grove, J. *et al.* Flat clathrin lattices: stable features of the plasma membrane. *MBoC* **25**, 3581–3594 (2014).

87. Horcas, I. *et al.* WSXM : A software for scanning probe microscopy and a tool for nanotechnology. *Rev. Sci. Instrum.* **78**, 013705 (2007).

88. Russo, C. J., Scotcher, S. & Kyte, M. A precision cryostat design for manual and semi-automated cryo-plunge instruments. *Rev. Sci. Instrum.* **87**, 114302 (2016).

89. Wagner, F. R. *et al.* Preparing samples from whole cells using focused-ion-beam milling for cryo-electron tomography. *Nat. Protoc.* **15**, 2041–2070 (2020).

ARTICLE IN PRESS

ARTICLE IN PRESS

90. Ganeva, I. *et al.* The architecture of Cidec-mediated interfaces between lipid droplets. *Cell Rep.* **42**, 112107 (2023).

91. Hagen, W. J. H., Wan, W. & Briggs, J. A. G. Implementation of a cryo-electron tomography tilt-scheme optimized for high resolution subtomogram averaging. *J. Struct. Biol.* **197**, 191–198 (2017).

92. Mastronarde, D. N. & Held, S. R. Automated tilt series alignment and tomographic reconstruction in IMOD. *J. Struct. Biol.* **197**, 102–113 (2017).

93. Kremer, J. R., Mastronarde, D. N. & McIntosh, J. R. Computer Visualization of Three-Dimensional Image Data Using IMOD. *J. Struct. Biol.* **116**, 71–76 (1996).

94. Castaño-Díez, D., Kudryashev, M., Arheit, M. & Stahlberg, H. Dynamo: A flexible, user-friendly development tool for subtomogram averaging of cryo-EM data in high-performance computing environments. *J. Struct. Biol.* **178**, 139–151 (2012).

95. Castaño-Díez, D., Kudryashev, M. & Stahlberg, H. Dynamo Catalogue: Geometrical tools and data management for particle picking in subtomogram averaging of cryo-electron tomograms. *J. Struct. Biol.* **197**, 135–144 (2017).

96. Espadas, J. *et al.* Dynamic constriction and fission of endoplasmic reticulum membranes by reticulon. *Nat. Commun.* **10**, 5327 (2019).

97. Rigaud, J.-L., Pitard, B. & Levy, D. Reconstitution of membrane proteins into liposomes: application to energy-transducing membrane proteins. *Biochim. Biophys. Acta - Bioenerg.* **1231**, 223–246 (1995).

Acknowledgments

We are grateful to Jean Gruenberg, Stefania Vossio, and Elina Ikonen for thoughtful discussions about the role of cholesterol in vesicle trafficking. Andrea Picco is acknowledged for technical support in

ARTICLE IN PRESS

TIRF imaging, and Rafael Ferreira Caetano and Frédéric Humbert for protein purification. We thank Roux and Kaksonen labs for technical support and helpful discussions. We thank the Photonic Light Microscopy Facility and ACCESS Facility at the University of Geneva, the Microscopy Imaging Center (MIC) of the University of Bern, the Dubochet Center for Imaging (DCI) Bern, the Light Microscopy Unit (LMU) at the Institute of Biotechnology at the University of Helsinki, and IBPS electron microscopy platform at Sorbonne University in Paris for microscope access and support with data collection.

Funding

This work was supported by EMBO (ALTF 703-2020 for M.H., and 989-2022 for J.E.), Research Council of Finland (grant 369982 for M.H.) Fundación Alfonso Martín Escudero (Postdoctoral fellowship for C.B-S.), and Swiss National Science Foundation grant (310030_212288) for Ma.K. A.R. acknowledges funding from the Swiss National Fund for Research grant numbers #CRSII5_189996 and #310030_200793 and the European Research Council Synergy grant number #951324-R2-TENSION. Work in the group of W.K. was supported by the University of Bern and the SNSF project 201158. We would also like to acknowledge funding by the *Agence Nationale pour la Recherche* (ANR-20-CE13-0024-01, ANR-21-CE13-0018-01 to SV), Horizon Europe DREAMS project under grant agreement N°101080229, Sorbonne Université, INSERM, Association Institut de Myologie core funding to S.V. Mi.K. is supported by the Helmholtz Society and the Heisenberg Award from the DFG (KU3222/3-1). A.C. Acknowledges PID2022-140687NB-I00 funded by MCIN/AEI /10.13039/501100011033/ and European Union Unión Europea Next GenerationEU/ PRTR, CNS2024-154624 founded by MICIU/AEI/10.13039/501100011033 CNS2024-154624, MICIU/AEI/10.13039/501100011033 and the Basque Resource for Advanced Light Microscopy (BRALM) located at Instituto Biofisika (CSIC, EHU) for their support and assistance in this work.

Author contribution statement

M.H., S.B.M., I.G., M.G., C.B.S., J.E., C.M., A.C., and S.V. carried out experiments and data analysis. Mi.K., W.K., A.C., S.V., Ma.K., and A.R. contributed to experiment planning and supervised the work. M.H., Ma.K., and A.R. conceived the study and planned experiments. M.H. and A.R. wrote the manuscript with input from all authors.

ARTICLE IN PRESS

Competing Interests Statement

The authors declare no competing interests

ARTICLE IN PRESS

ARTICLE IN PRESS

Figure legends

Figure 1. HRS forms two-dimensional condensates on membranes

a, Fluorescence spinning disk confocal microscope images of GUVs (magenta) with and without 1% PI(3)P incubated 30 minutes with 250 μM labelled HRS (green). Scale bars are 5 μm. The a. u. is the abbreviation of arbitrary units. **b,** a representative example of a TIRF microscopy time-lapse montage of SLBs (magenta) incubated with 250 nM labelled HRS (green). Scale bar is 5 μm. **c**, The recruitment of 100 nM, 250 nM, and 500 nM HRS on 1% PI(3)P-rich SLB. Data is a mean of four measurements with a standard deviation shown. The experiment was repeated three times with similar results. **d,** Examples of HRS droplet condensate fusion. Scale bar is 2 μm. **e,** Example of time-lapse images of HRS droplets after photobleaching. Scale bar is 5 μm. The experiment was repeated five times. **f,** A TIRF microscopy time-lapse montage of HRS droplets (green) spreading on the SLB membrane (magenta). The experiment was repeated four times. **g,** A TIRF microscopy time-lapse montage of 2μM bulk HRS (green) nucleating two-dimensional condensate formation on SLB (magenta). Scale bars in f-g are 10 μm. The experiment was repeated four times. **h,** Representative examples of 10 μM and 20 μM labeled HRS (green) on GUV membrane (magenta). Scale bars are 5 μm. The experiment was repeated three times. Source data are provided as a Source Data file.

Figure 2. The C-terminal tail and the helical domain of HRS promotes phase separation

a, A time-lapse montage of high-speed AFM of 500 nM HRS recruitment on SLBs. Scale bar is 500 nm. The border between SLB membrane and bare mica is indicated with a red dashed line. **b**, A histogram of HRS coat thicknesses (black) in the AFM data in panel a. Each event represents a pixel on SLB. The thickness of the protein coat is indicated with a membrane surface as a value 0 nm (red). **c,** A domain structure of human HRS. VHS, FYVE, DUIM, and helical domains as well as CB (clathrin box motif), are shown. A FuzDrop prediction of human HRS. Droplet-formation probability (P_{DP}) over residue number is shown. A ParSe 2.0 prediction of human HRS phase-separation. Residue-level prediction for folded (black dots), disorder but no phase separation (red dots) and phase separating (blue dots) regions are shown. **d,** A representative widefield microscope images of HeLa MZ cells transiently expressing GFP-HRS plasmids. Construct numbering refers to HRS regions as indicated in panel c. Scale bars are 10 μm. Experiments were repeated four times with similar results. **e,** An example of GFP-HRS 1-777 protein droplet fusions (indicated with arrow heads) in HeLa cells.

ARTICLE IN PRESS

Scale bar is 3 μm. **f,** colocalization of GFP-HRS 1-777 protein droplets (green) with endosome marker (EGF AlexaFluor 647, magenta). The experiment was repeated three times with similar results. Scale bars are 10 μm for the large image and 3 μm for the zoom-in. Source data are provided as a Source Data file.

Figure 3. HRS recruits clathrin on membranes as flat patches and spherical cages

a, A schematic illustration of the reconstitution strategy on SLBs using sequential protein addition. **b**, A representative example of the recruitment of 200 nM clathrin (20% AlexaFluor-488 labeled, cyan) over time on SLBs (magenta) preincubated with 500 nM nonlabelled HRS imaged with a TIRF microscope. The scale bar is 10 μm. **c**, The recruitment of 200 nM clathrin (20% AlexaFluor-488 labeled) over time with different HRS concentrations. Data is the mean of four experiments with standard deviations shown. The experiment was repeated three times. The a. u. is the abbreviation of arbitrary units. **d-e**, Nucleation rates (initial assembly rate) (**d**) and final clathrin fluorescence intensities (**e**) plotted over HRS concentration from the data in panel c. Data represents four measurements with individual data points shown. In the box plot, the line indicates a median value, the box 25^{th} and 75^{th} percentiles and whiskers 5^{th} and 95^{th} percentiles. **f-g**, Representative PREM images of reconstituted HRS-clathrin lattices on SLBs. Two different HRS concentrations were used: (**f**) 100 nM HRS and (**g)** 500 nM HRS, with clathrin concentration being 200 nM in both samples. The orange scattered line indicates the border between regions containing domes and flat coats. Scale bars in panels f-g for larger images are 300 nm, and for zoom-in images 50 nm. The experiment was repeated twice. **h**, Representative HS-AFM images of HRS and HRS-clathrin coats on SLBs. The scale bar is 500 nm. **i**, A histogram of HRS (n=2 samples) and HRS-clathrin (n=5) coat thicknesses. Each event represents a pixel on SLB. Statistical tests in panels d-e are the two-tailed Welch's t-test. Source data are provided as a Source Data file.

Figure 4. HRS and clathrin form multilayered protein coats in vitro.

ARTICLE IN PRESS

a, Representative PREM images of reconstituted, multilayered HRS-clathrin lattices on SLBs. Concentrations of HRS and clathrin are 500 nM and 200 nM, respectively. Scale bars in panel a are 1 μm for the left image, 300 nm for the first zoom-in, and 50 nm for the second zoom-in image. Experiment was repeated twice. **b**, Representative images of reconstituted 1 μM HRS and 200 nM clathrin lattices on supported lipid bilayers (SLBs), captured using PREM. The PREM image reveals clathrin lattices with varying layer numbers (two, three, and four layers). Scale bar is 1 μm. Experiment was repeated twice. **c**, Quantification of electron opacity of different clathrin layers as indicated in panel c. The histogram represents pooled data from multiple ROIs across three independent experiments. Statistical significance was assessed using a two-tailed t-test. In the box plot, the line indicates a median value, the box 25th and 75th percentiles and whiskers 5th and 95th percentiles. **d,** A representative example of two-dimensional condensate after 1 μM HRS was incubated on SLBs. Scale bars are 300 nm and 100 nm (zoom-in). Experiment was repeated twice. Statistical tests in panel c are the two-tailed Welch's t-test. Source data are provided as a Source Data file.

ARTICLE IN PRESS

Figure 5. Clathrin assembles as dome-like structures on HRS droplet condensates

a, Representative PREM images of clathrin coat reconstituted on HRS droplet condensates. SLBs were incubated with 2 μM HRS and 200 nM clathrin. Scale bars from left to right: 5 μm, 1 μm, 500 nm. The experiment was repeated twice. **b**, Representative PREM image of clathrin coat next to droplet HRS condensate. SLBs were incubated with 2 μM HRS and 200 nM clathrin. Scale bars are 300 nm for the larger image and 100 nm for the zoom-in. The experiment was repeated twice. **c**, A schematic illustration of four different HRS-clathrin coat structures observed in reconstituted samples. Low-density HRS yields a sparse clathrin coat. Two-dimensional HRS condensates lead to a mixture of flat and dome-like clathrin coats. Droplet-like HRS condensate promotes the assembly of dome-like and spherical clathrin coats on the surface of the HRS condensate.

Figure 6. Clathrin assembles as a hexagonal lattice on endosomes

a, A representative cryo-electron tomogram from in total 12 tomograms of endosomes with putative HRS-clathrin coat patches, indicated by yellow brackets. Areas magnified in panels b and c are indicated by yellow rectangles. White labels indicate some identified cellular components:

ARTICLE IN PRESS

E=endosome, ER=endoplasmic reticulum, L=lysosome, M=mitochondrium, MT=microtubules. Scale bar is 250 nm. **b-c**, Close-ups of protein coats on endosome membranes in a tomogram from panel a. Arrows point to the multiple layers within the coats. Scale bars are 50 nm. **d-f**, Subtomogram averaging. In total eight tomograms were used in processing. **d-e**, A density profile and side view of the membrane and protein layers with distances between the layers indicated. Scale bar is 20 nm. **f**, A top view of layer 1 (perpendicular to view in e), shown as a slice through the volume and as an isosurface (blue), revealing the hexagonal lattice structure. Scale bar is 40 nm.

Figure 7. Cholesterol promotes endosomal localization of HRS in cells

a, Representative maximum projection images from confocal fluorescence microscopy stack images of mScarlet-I3-HRS (magenta) CRISPR knock-in cell lines with filipin staining (green). The scale bar is 20 μm for larger images and 2 μm for zoom-in images. The experiment was repeated three times. **b**, Filipin staining (yellow) in HeLa wild-type cells and NPC1 knockout cells showing enrichment of cholesterol at endo-lysosomal membranes. Scale bars are 10 μm. The experiment was repeated three times with similar results. **c**, Representative immunofluorescence confocal microscopy images of HRS (magenta) and clathrin (green) in HeLa wild-type cells and HeLa NPC1 knockout cells. Scale bars are 10 μm. **d-f**, High content image analysis of HRS mean intensity in cells (**d**), HRS mean patch size in cells (**e**), and clathrin mean intensity in HRS patches in cells (**f**). Each data point represents the mean of the image with median values, 25% and 75% percentiles, and the range of data indicated. Experiment was repeated three times. Statistical tests in panels d-f are the two-tailed Welch's t-test. The a. u. is the abbreviation of arbitrary units. Source data are provided as a Source Data file.

Figure 8. Cholesterol enhances the recruitment of HRS onto the membrane *in vitro*

a, Representative fluorescence microscopy images of PI(3)P-rich GUVs (magenta) with indicated cholesterol concentrations and 500 nM labeled HRS (cyan). Scale bars are 5 μm. **b**, Representative fluorescence microscopy images of PI(3)P-rich GUVs (magenta) with indicated cholesterol concentrations and 500 nM nonlabelled HRS and 200 nM clathrin (20% labeled, cyan). Scale bars are 5 μm. **c**, The analysis of fluorescence intensity of labeled HRS on GUV membrane (panel a) with different cholesterol concentrations. Each data point represents an individual GUV. The experiment

ARTICLE IN PRESS

was repeated three times. **d**, The analysis of fluorescence intensity of labeled clathrin on GUV membrane (panel b) with different cholesterol concentrations. Each data point represents an individual GUV. The experiment was repeated three times. In panels c-d, the a. u. is the abbreviation of arbitrary units. **e**, Representative fluorescence microscopy images of 2 μM labeled HRS (cyan) on PI3P-rich SLBs (magenta) with varying cholesterol concentrations. N=5 experiments for 0% and 30% cholesterol samples, and N=6 for 15% cholesterol samples. The scale bar is 50 μm. **f**, The percentage labeled HRS-covered SLBs with different cholesterol concentrations. Each data point represents a mean coverage value in one sample. N=5 experiments for 0% and 30% cholesterol samples, and N=6 for 15% cholesterol samples. **g**, Representative fluorescence microscopy images of GUVs first incubated with 500 nM HRS and 200 nM clathrin and subsequently brought into +50 mOsm osmolarity (hyperosmotic shock). Scale bars are 5 μm. The experiment was repeated three times. **h**, A representative example of flattened GUV membranes containing 30% cholesterol and incubated with 500 nM HRS and 200 nM clathrin before 50 mOsm osmotic shocks. Equatorial plane images and maximum projection images are shown. Scale bars are 5 μm. In panels c, d, and f, each data point represents an individual measurement with median values, 25% and 75% percentiles, and the range of data indicated. Experiments were repeated three times. Statistical tests in panels c, d, and f are the two-tailed Welch's t-test. Source data are provided as a Source Data file.

ARTICLE IN PRESS

Figure 9 Cholesterol concentrates under the HRS-clathrin coat

a, A schematic presentation of the fluorescence quenching assay. **b**, TopFluor-cholesterol fluorescence spectra with different HRS concentrations. The experiment was repeated three times. **c**, TopFluor-cholesterol sorting coefficient analysis with HRS or HRS and clathrin. A representative fluorescence microscopy image of 1% TopFluor-cholesterol (yellow) in SLB incubated with 2 μM HRS (unlabeled) and 200 nM clathrin (20% AF-568 labeled, magenta). The scale bar is 5 μm. Sorting coefficient values were plotted for 2 μM HRS alone and 2 μM HRS + 200 nM clathrin samples. Each data point represents sorting coefficient measurements on an independent SLB from three experiments. **d-f**, FRAP experiments to measure TopFluor-cholesterol diffusion in control samples (no proteins), with 500 nM HRS, and with 500 nM HRS and 200 nM clathrin. **d**, Recovery curves of TopFluor-cholesterol after photobleaching in control samples (grey) and in the presence of HRS (green), and HRS and clathrin (orange). Dark lines represent mean values, and shaded areas represent

ARTICLE IN PRESS

standard deviations. **e**, Percentage of immobile fraction of TopFluor-cholesterol FRAP experiment. **f**, Recovery halftimes of TopFluor-cholesterol FRAP experiments. In panels e-f, each data point represents an independent measurement from in total of three experiments. In box plots in panels c, e, and f, the line indicates a median value, the box 25^{th} and 75^{th} percentiles and whiskers 5^{th} and 95^{th} percentiles. The statistical test in panel c is the two-tailed Welch's t-test. Statistical tests in panels e-f are the two-tailed Kruskal-Wallis test. Source data are provided as a Source Data file.

Figure 10. HRS clusters ubiquitylated cargoes in a cholesterol-dependent manner

a, A schematic illustration of reconstitution (see Methods, Cargo protein reconstitution and clustering, for details) of 4xubiquitin-VAMP2-sfGFP cargo protein into GUV membrane. The illustration was in BioRender. Hakala, M. (2026) https://BioRender.com/fntq0zg **b**, Representative fluorescence microscopy images of 4xubiquitin-VAMP2-sfGFP (cyan) reconstituted on GUV membrane (grey) containing either 1% PI(3)P/30% cholesterol or 1% PI(3)P/no cholesterol before the addition of HRS. The scale bar is 5 μm. **c**, Representative fluorescence microscopy images of 4xubiquitin-VAMP2-sfGFP (cyan) reconstituted on GUV membrane (grey) containing either 1% PI(3)P/30% cholesterol or 1% PI(3)P/no cholesterol after addition of 500 nM mScarlet-I3-HRS (magenta). The scale bar is 5 μm. The experiment was repeated four times. **d-e,** Kymographs of GUV membranes showing the mobility of HRS-VAMP2 clusters on membrane with 30% cholesterol (panel e) and without cholesterol (panel d). **f**, A model of HRS and clathrin assembly on PI(3)P-rich and cholesterol-rich membranes. HRS binds to PI(3)P through its FYVE domain. Binding is weak in the absence of cholesterol. Cholesterol promotes HRS recruitment on membrane, and HRS forms two-dimensional condensates. HRS condensates concentrates cholesterol under the protein coat. Clathrin assembles on HRS condensate to form a multilayered protein coat, leading to a mixture of flat and curved clathrin coats. Cholesterol-rich, stable membrane domain under the protein coat promotes the clustering of ubiquitinated cargo proteins.

ARTICLE IN PRESS

The ESCRT-protein HRS undergoes two-dimensional phase separation on endosomal membranes to form gel-like condensates that recruit clathrin into multilayered, flat coats. Cholesterol enhances this process and drives stable cargo-sorting microdomains

Peer review information: *Nature Communications* thanks Gijsje Koenderink, and the other, anonymous, reviewer(s) for their contribution to the peer review of this work. A peer review file is available.

ARTICLE IN PRESS

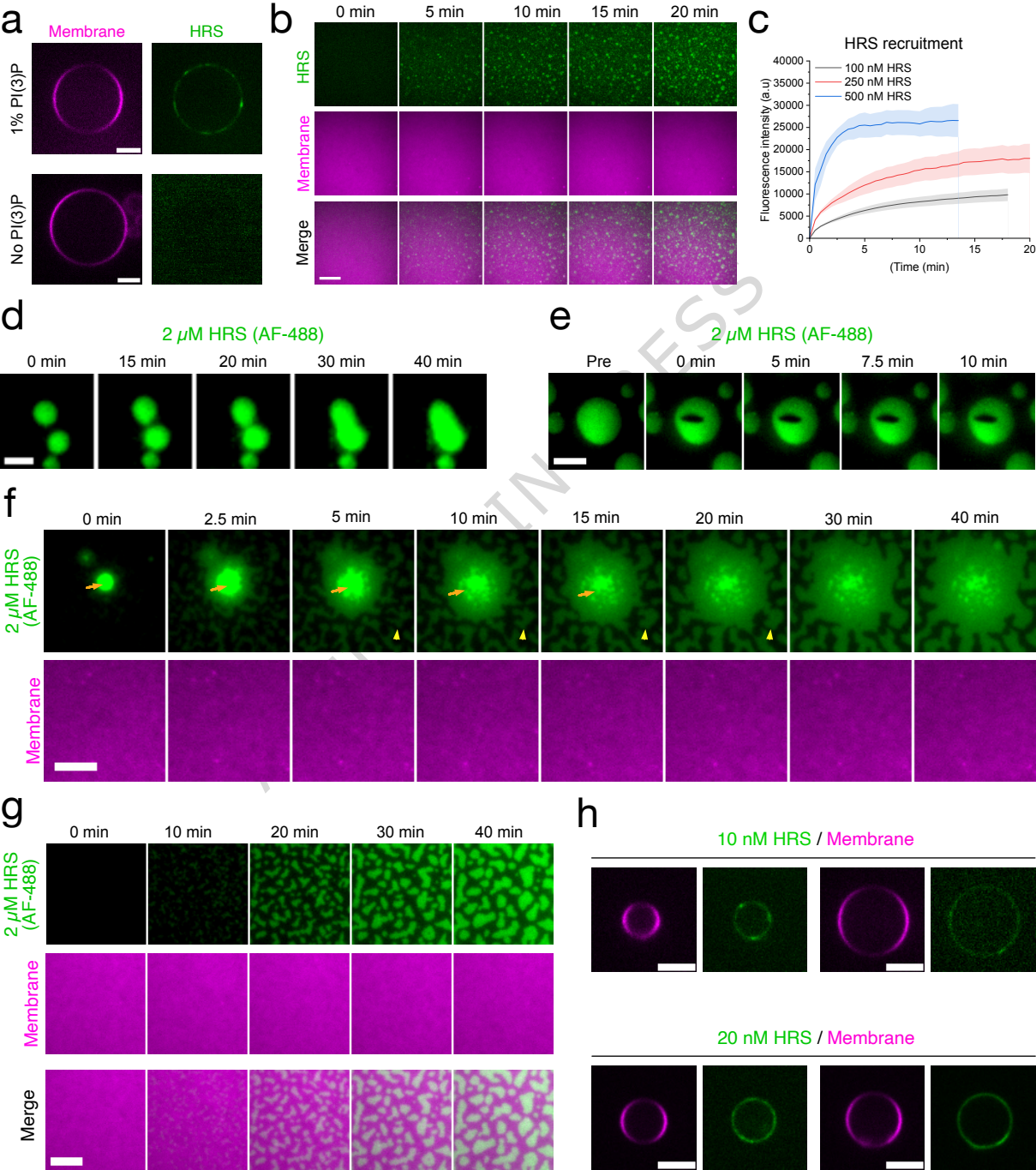
a
Membrane
HRS
1% PI(3)P
No PI(3)P
b
0 min
5 min
10 min
15 min
20 min
HRS
Membrane
Merge
c
HRS recruitment
100 nM HRS
250 nM HRS
500 nM HRS
Fluorescence intensity (a.u)
(Time (min)
d
2 μM HRS (AF-488)
0 min
15 min
20 min
30 min
40 min
e
2 μM HRS (AF-488)
Pre
0 min
5 min
7.5 min
10 min
f
0 min
2.5 min
5 min
10 min
15 min
20 min
30 min
40 min
2 μM HRS (AF-488)
Membrane
g
0 min
10 min
20 min
30 min
40 min
2 μM HRS (AF-488)
Membrane
Merge
h
10 nM HRS / Membrane
20 nM HRS / Membrane

ARTICLE IN PRESS

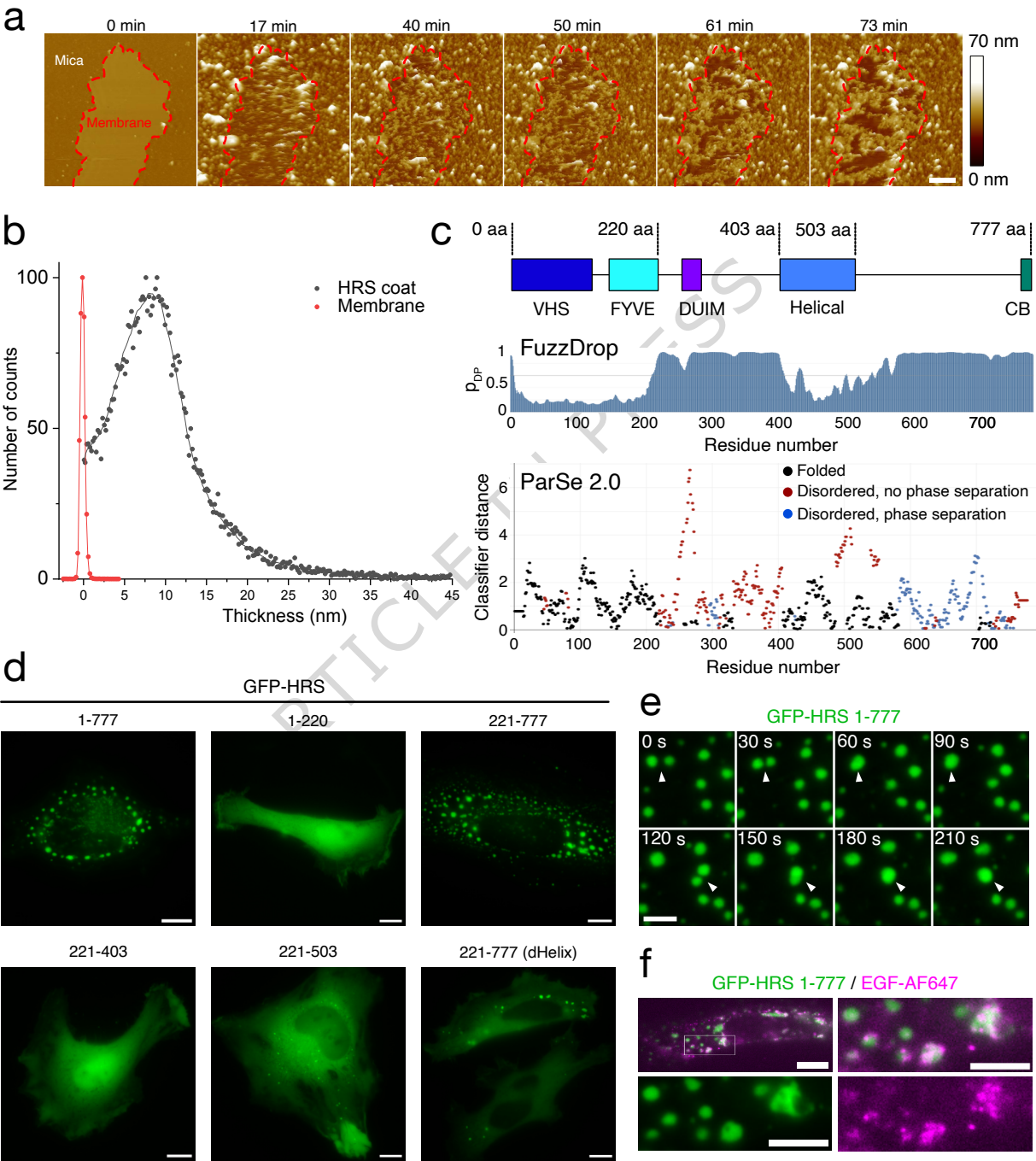

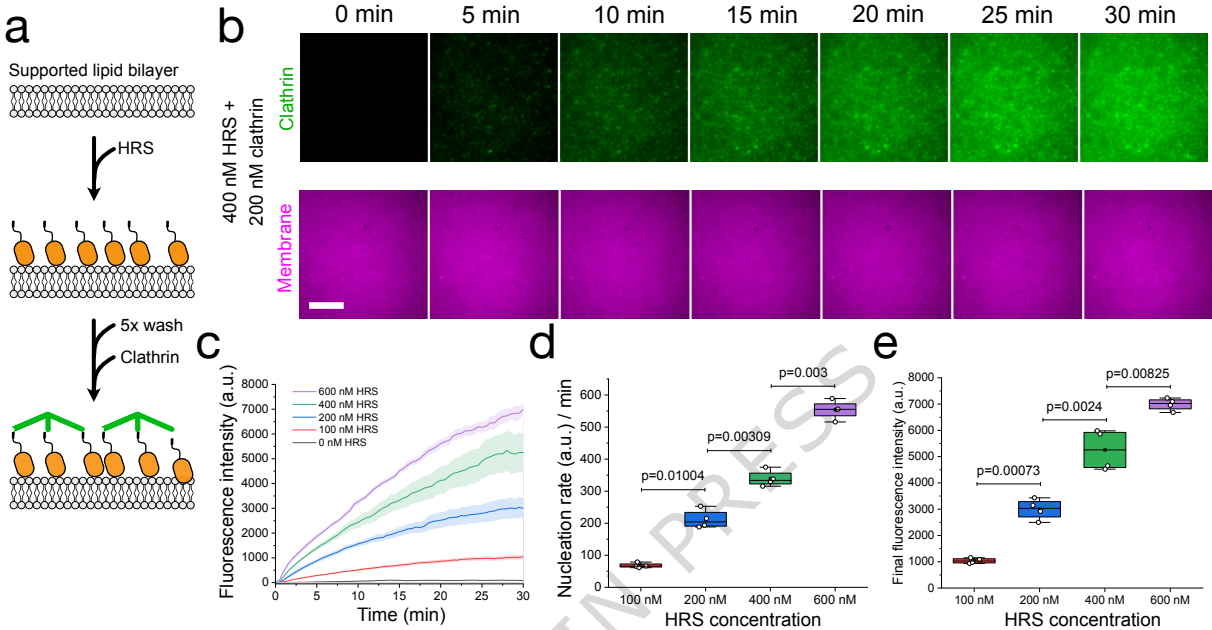
a
Supported lipid bilayer
HRS
5x wash
Clathrin
b
0 min
5 min
10 min
15 min
20 min
25 min
30 min
400 nM HRS +
200 nM clathrin
Clathrin
Membrane
c
Fluorescence intensity (a.u.)
600 nM HRS
400 nM HRS
200 nM HRS
100 nM HRS
0 nM HRS
Time (min)
d
Nucleation rate (a.u.) / min
p=0.01004
p=0.00309
p=0.003
100 nM
200 nM
400 nM
600 nM
HRS concentration
e
Final fluorescence intensity (a.u.)
p=0.00073
p=0.0024
p=0.00825
100 nM
200 nM
400 nM
600 nM
HRS concentration

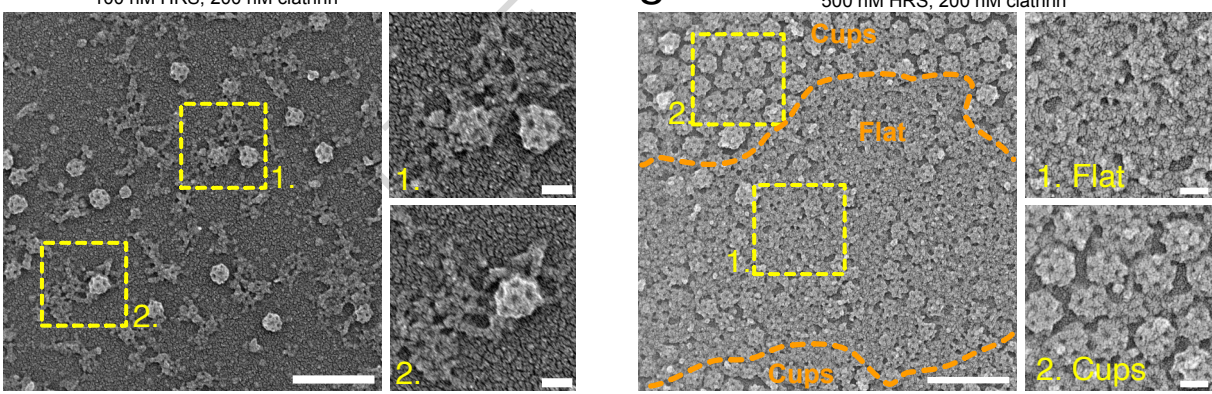
f
100 nM HRS, 200 nM clathrin
1.
2.
g
500 nM HRS, 200 nM clathrin
Cups
Flat
1.
2.
1. Flat
2. Cups

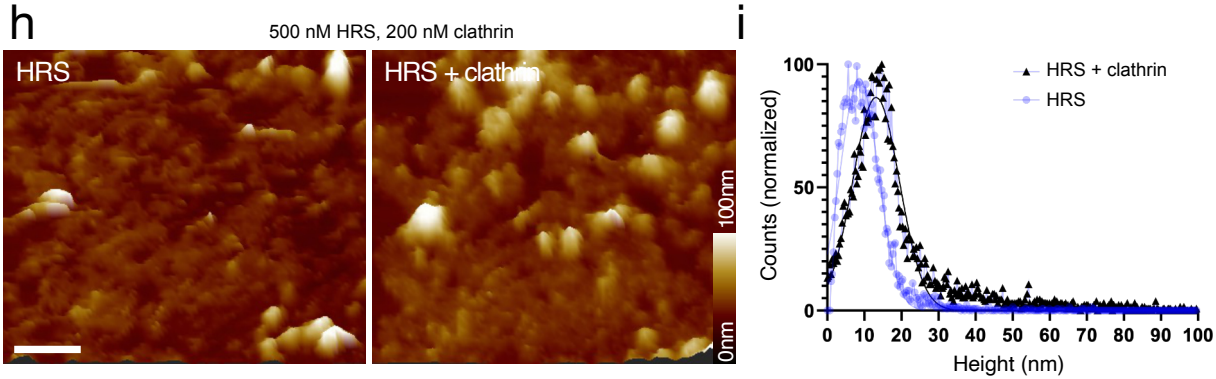
h
500 nM HRS, 200 nM clathrin
HRS
HRS + clathrin
100nm
0nm
i
HRS + clathrin
HRS
Counts (normalized)
Height (nm)

ARTICLE IN PRESS

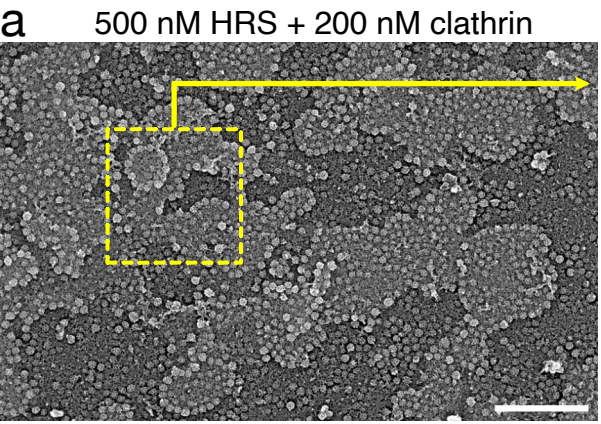

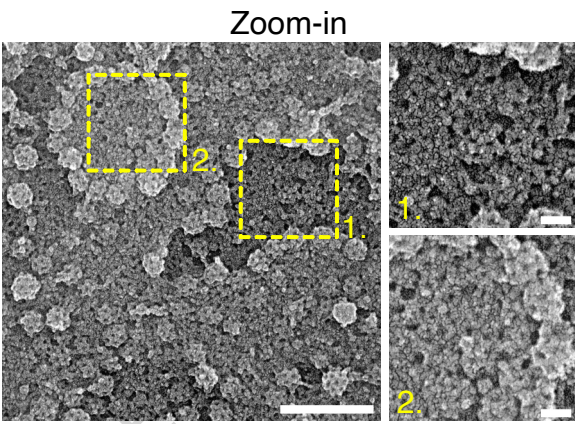

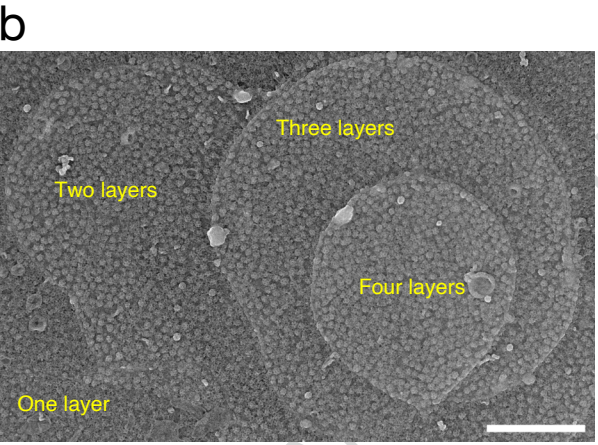

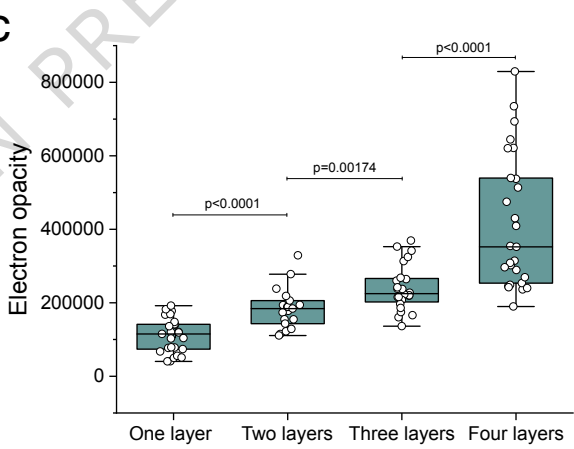

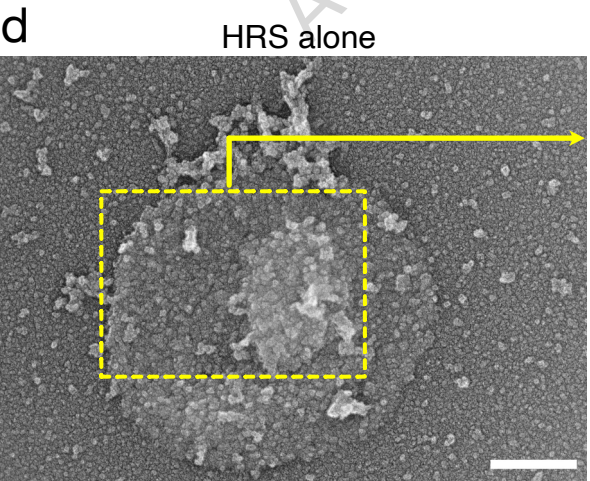

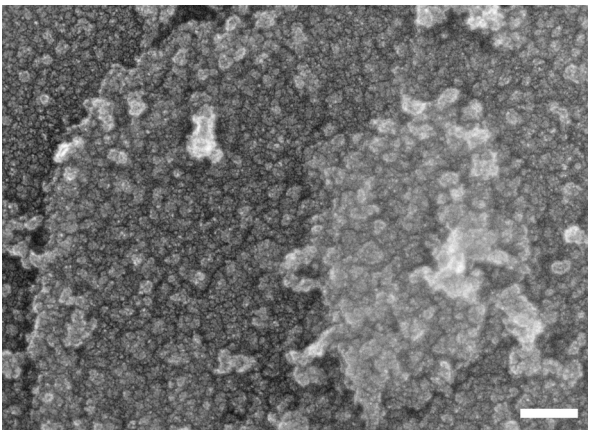

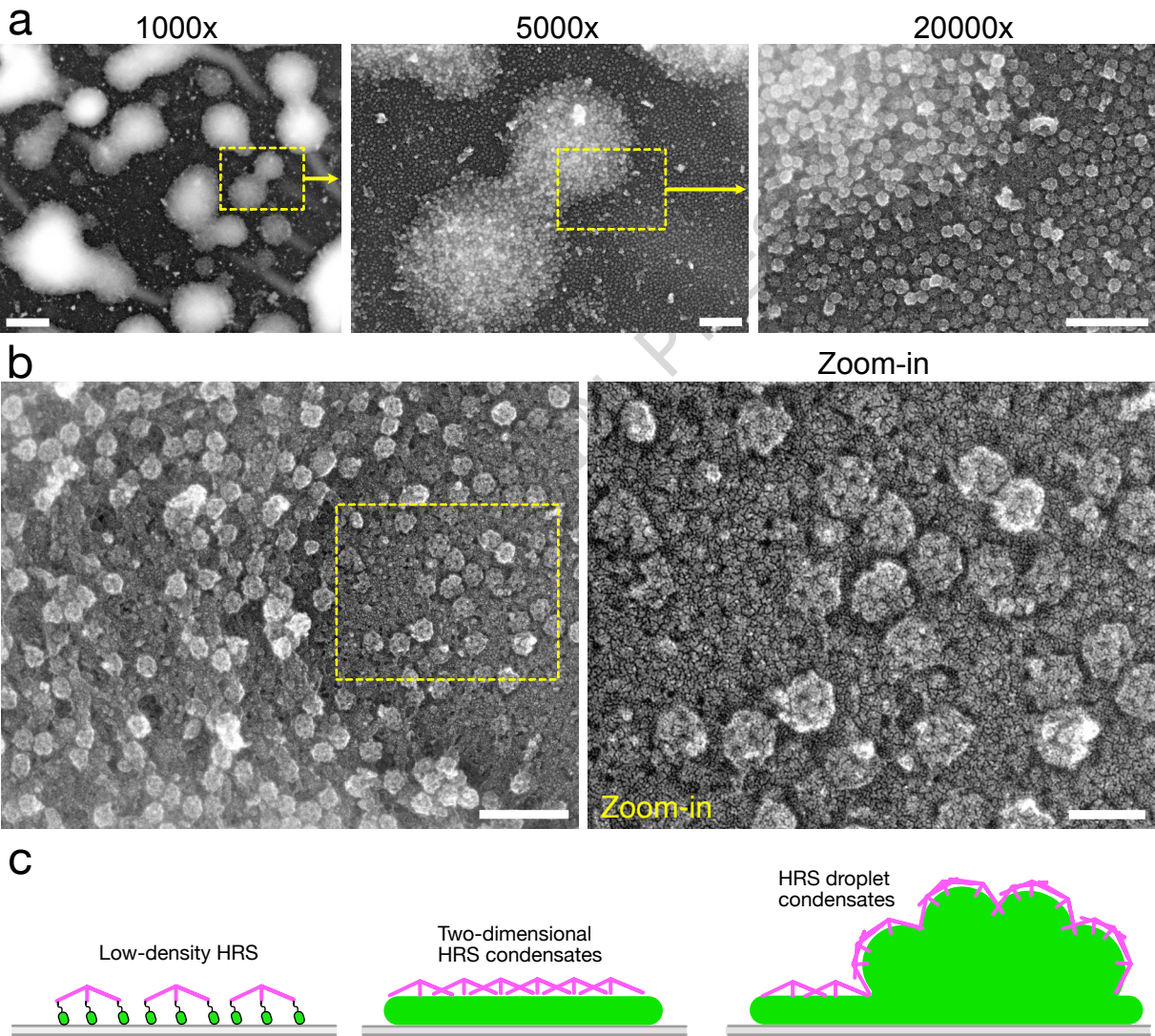
a
1000x
5000x
20000x
b
Zoom-in
Zoom-in
c
Low-density HRS
Two-dimensional
HRS condensates
HRS droplet
condensates

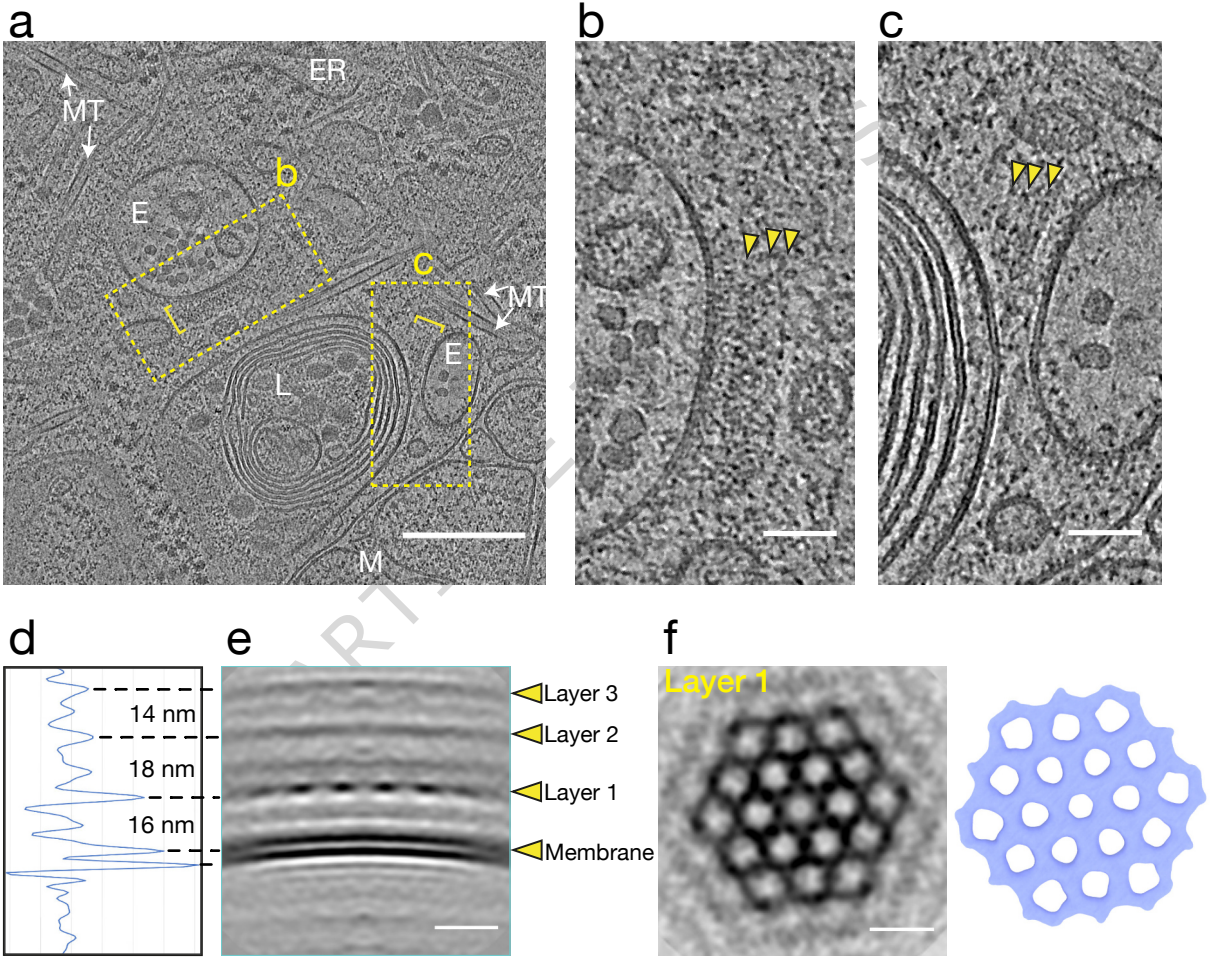
a
ER
MT
b
E
c
MT
L
E
L
M
b
c
d
14 nm
18 nm
16 nm
e
Layer 3
Layer 2
Layer 1
Membrane
f
Layer 1

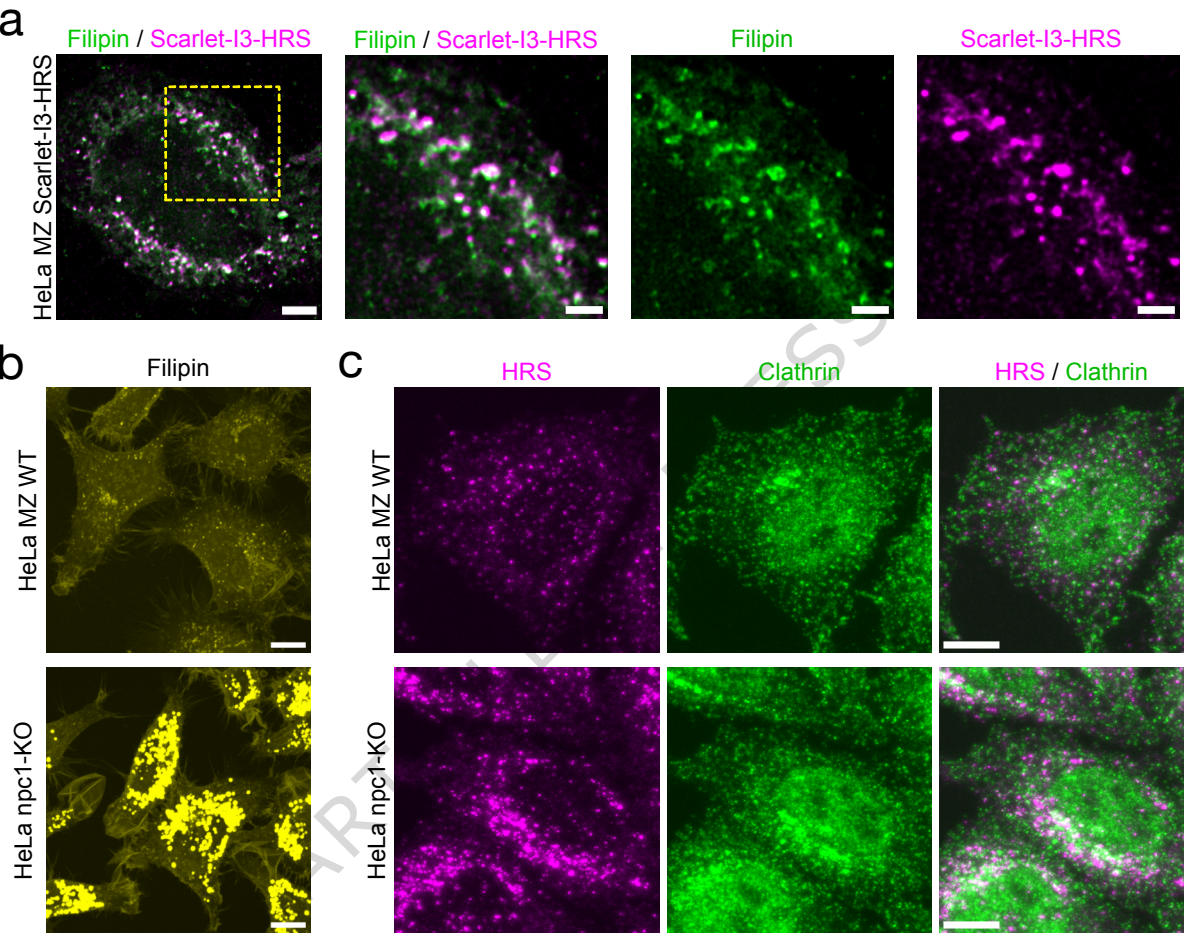
a
Filipin / Scarlet-I3-HRS
Filipin / Scarlet-I3-HRS
Filipin
Scarlet-I3-HRS
HeLa MZ Scarlet-I3-HRS
b
Filipin
HeLa MZ WT
HeLa npc1-KO
c
HRS
Clathrin
HRS / Clathrin
HeLa MZ WT
HeLa npc1-KO

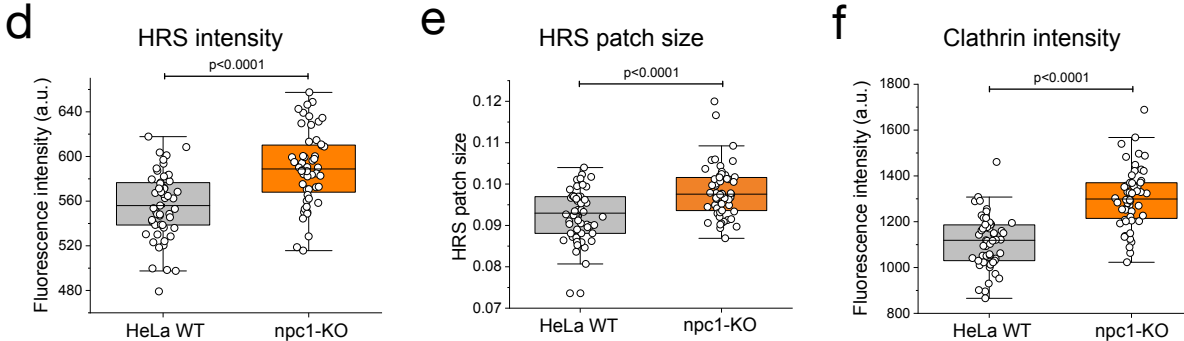
d
HRS intensity
p<0.0001
Fluorescence intensity (a.u.)
640
600
560
520
480
HeLa WT
npc1-KO
e
HRS patch size
p<0.0001
HRS patch size
0.12
0.11
0.10
0.09
0.08
0.07
HeLa WT
npc1-KO
f
Clathrin intensity
p<0.0001
Fluorescence intensity (a.u.)
1800
1600
1400
1200
1000
800
HeLa WT
npc1-KO

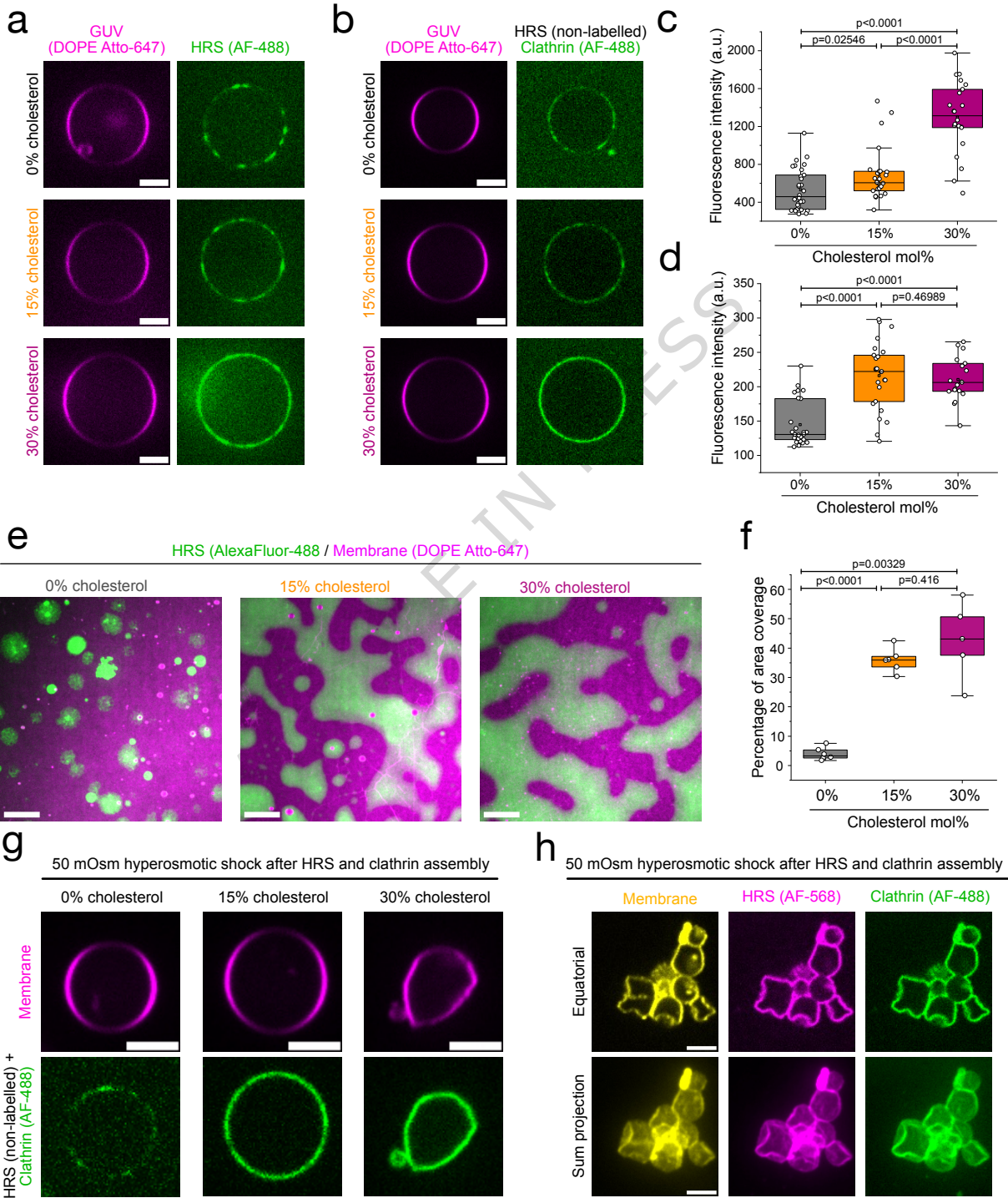
a
GUV (DOPE Atto-647)
HRS (AF-488)
0% cholesterol
15% cholesterol
30% cholesterol
b
GUV (DOPE Atto-647)
HRS (non-labelled) Clathrin (AF-488)
0% cholesterol
15% cholesterol
30% cholesterol
c
p<0.0001
p=0.02546
p<0.0001
Fluorescence intensity (a.u.)
2000
1600
1200
800
400
0%
15%
30%
Cholesterol mol%
d
p<0.0001
p<0.0001
p=0.46989
Fluorescence intensity (a.u.)
350
300
250
200
150
100
0%
15%
30%
Cholesterol mol%
e
HRS (AlexaFluor-488 / Membrane (DOPE Atto-647)
0% cholesterol
15% cholesterol
30% cholesterol
f
p=0.00329
p<0.0001
p=0.416
Percentage of area coverage
60
50
40
30
20
10
0
0%
15%
30%
Cholesterol mol%
g
50 mOsm hyperosmotic shock after HRS and clathrin assembly
0% cholesterol
15% cholesterol
30% cholesterol
Membrane
HRS (non-labelled) + Clathrin (AF-488)
h
50 mOsm hyperosmotic shock after HRS and clathrin assembly
Membrane
HRS (AF-568)
Clathrin (AF-488)
Equatorial
Sum projection

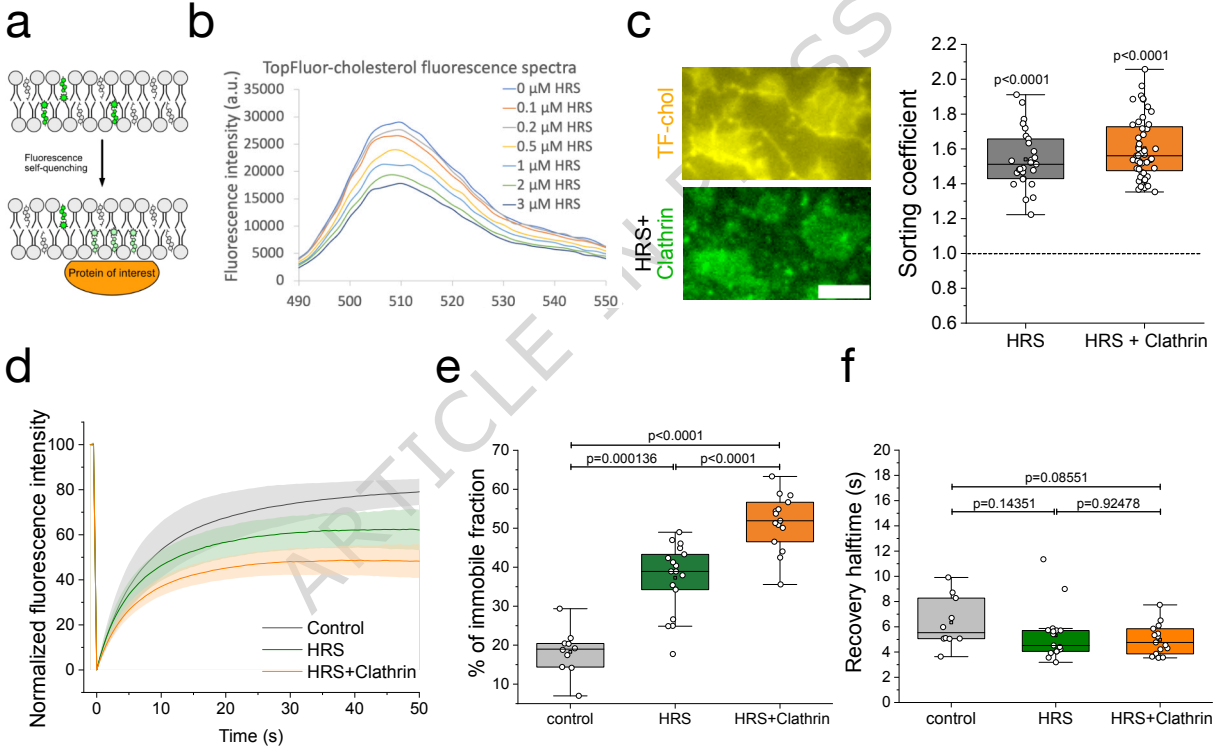
a
Fluorescence self-quenching
Protein of interest
b
TopFluor-cholesterol fluorescence spectra
Fluorescence intensity (a.u.)
0 µM HRS
0.1 µM HRS
0.2 µM HRS
0.5 µM HRS
1 µM HRS
2 µM HRS
3 µM HRS
c
TF-chol
HRS+ Clathrin
Sorting coefficient
p<0.0001
p<0.0001
HRS
HRS + Clathrin
d
Normalized fluorescence intensity
Time (s)
Control
HRS
HRS+Clathrin
e
% of immobile fraction
p<0.0001
p=0.000136
p<0.0001
control
HRS
HRS+Clathrin
f
Recovery halftime (s)
p=0.08551
p=0.14351
p=0.92478
control
HRS
HRS+Clathrin

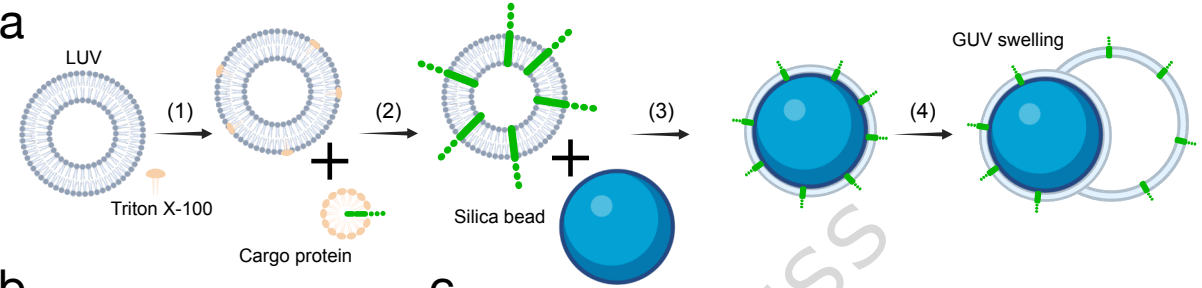
a
LUV
(1)
Triton X-100
(2)
Cargo protein
Silica bead
(3)
(4)
GUV swelling

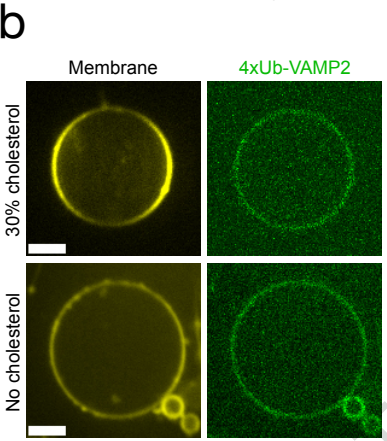
b
Membrane
4xUb-VAMP2
30% cholesterol
No cholesterol

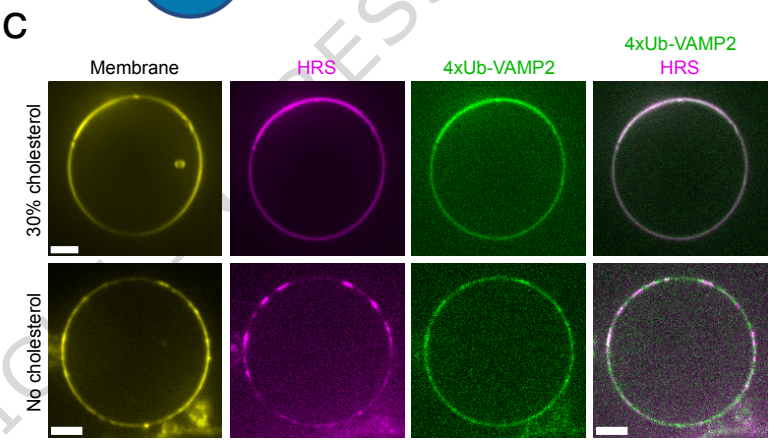
c
Membrane
HRS
4xUb-VAMP2
4xUb-VAMP2
HRS
30% cholesterol
No cholesterol

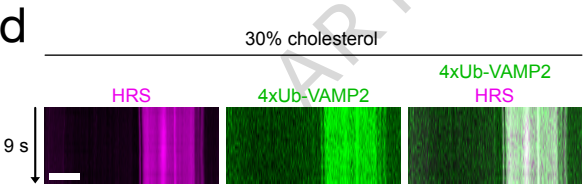
d
30% cholesterol
HRS
4xUb-VAMP2
4xUb-VAMP2
HRS
9 s

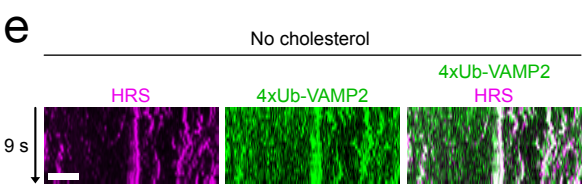
e
No cholesterol
HRS
4xUb-VAMP2
4xUb-VAMP2
HRS
9 s

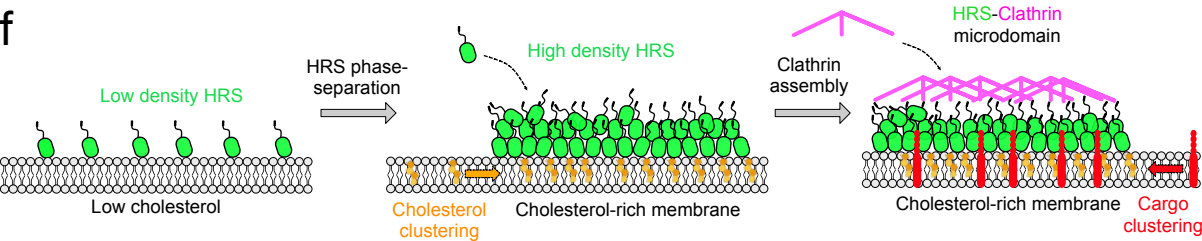
f
Low density HRS
Low cholesterol
HRS phase-separation
High density HRS
Cholesterol clustering
Cholesterol-rich membrane
Clathrin assembly
HRS-Clathrin microdomain
Cholesterol-rich membrane
Cargo clustering